This Document Provided by the Abbott Aerospace
Technical Library
abbottaerospace.com

Estimation of

Firewall Loads due to Soft Soil Impact

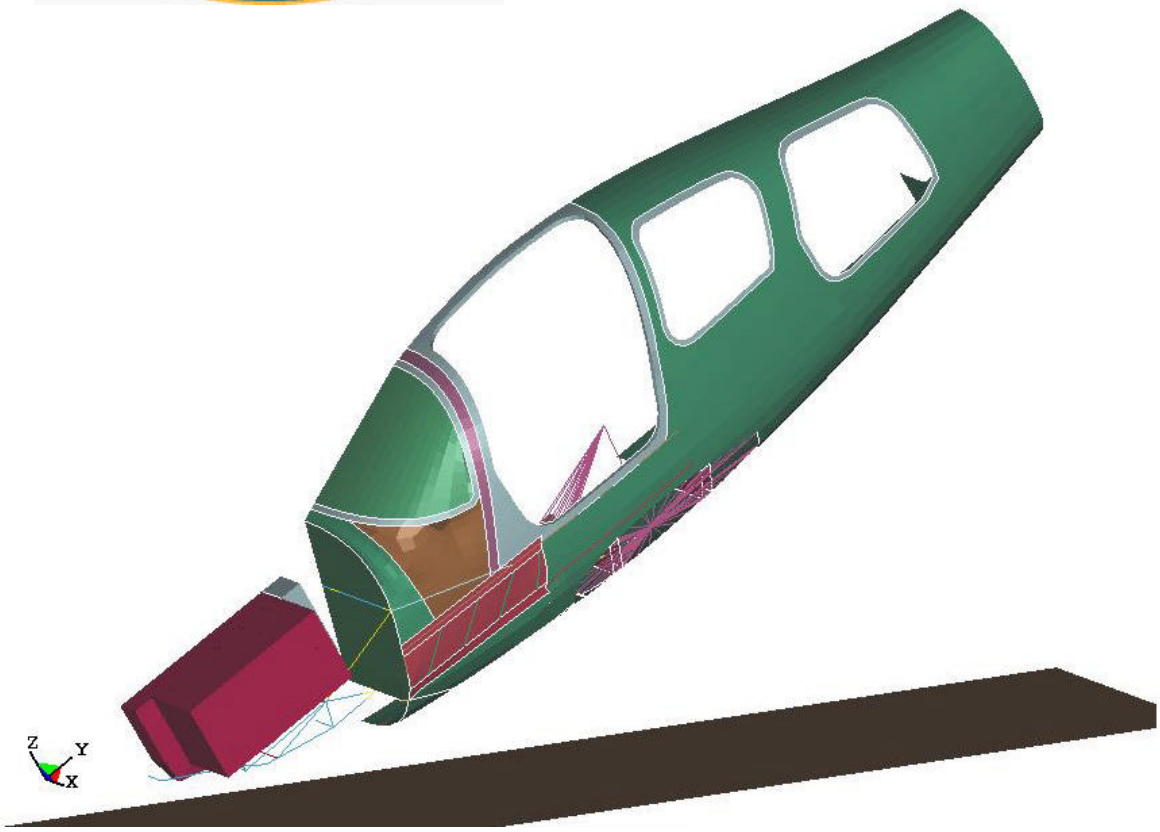

Marilyn Henderson
National Institute for Aviation Research
Wichita State University

Steven J. Hooper
J. B. Dwerlkotte Assoc., Inc.

Report Reference Number: AGATE-WP3.4-034026-087, Rev. A
Work Package Title: WBS3.0 Integrated Design and Manufacturing
Date of General Release: March 1, 2002

THIS DOCUMENT PROVIDED BY THE ABBOTT AEROSPACE
TECHNICAL LIBRARY
ABBOTTAEROSPACE.COM

Abstract

Emergency landings on soft soil represent one of the most severe impact conditions encountered during aircraft accidents. The loads generated during these events are of special interest to crashworthiness engineers since they are needed to design the structure forward of the firewall in order to mitigate the airframe accelerations. The cabin structure must also be sized for these loads to ensure that a survivable volume is maintained throughout the impact response.

All nose-down impacts are of interest, but those into soft soil represent the critical condition because of the potentially large longitudinal forces associated with the momentum transfer of the displaced soil. The nacelle and engine mount designs in aircraft with a conventional tractor propulsion configuration play an important role in aircraft response. Terry [1,2] demonstrated the feasibility of reducing the longitudinal decelerations produced during this impact condition by integrating appropriate load-deflection characteristics into a non-scooping design of an AGATE-class aircraft. The analysis described in this report extracts engine mount forces from these drop test data for use in the preliminary sizing of the engine mount and cabin structure. Future efforts will include their use in the validation of nonlinear finite element models of this problem.

THIS DOCUMENT PROVIDED BY THE ABBOTT AEROSPACE
TECHNICAL LIBRARY
ABBOTTAEROSPACE.COM

Table of Contents

THIS DOCUMENT PROVIDED BY THE ABBOTT AEROSPACE
TECHNICAL LIBRARY
ABBOTTAEROSPACE.COM

Figures

THIS DOCUMENT PROVIDED BY THE ABBOTT AEROSPACE
TECHNICAL LIBRARY
ABBOTTAEROSPACE.COM

Figures (continued)

THIS DOCUMENT PROVIDED BY THE ABBOTT AEROSPACE
TECHNICAL LIBRARY
ABBOTTAEROSPACE.COM

Introduction

The objective of the AGATE advanced crashworthiness research program was to significantly improve the level of occupant safety in accidents involving small general aviation aircraft. The program intended to develop the necessary technologies as well as design and certification processes that produce this enhanced level of safety.

A large number of full-scale pendulum-type drop tests of general aviation aircraft have been performed over the last 47 years [1-9]. Most of these tests utilized test articles that were designed in the 1960's and before. As such, they provided a great deal of useful data regarding what kind of responses to expect from these aircraft. Numerous analyses of the data generated have been performed. Soltis and Olcott [10] based part of the GASP committee's recommendations for the test pulses specified in the Emergency Landing Conditions specified in 14 CFR 23.562 on these results. The promulgation of this regulation, known as the dynamic seat test rule, was also motivated by the need to improve the crashworthiness of general aviation aircraft. The dynamic seat rule provides crashworthiness protection for general aviation aircraft certified after 1988 and specifies two dynamic test conditions: a combined (vertical/longitudinal velocity change) dynamic test condition and a second (longitudinal velocity change) dynamic test condition. The former is often critical for vertical spine loads and energy management in the seat frame, seat diaphragm, and cushion. The latter emphasizes the performance of the occupant/restraint/seat retention system and is generally critical for loads in the upper-torso restraint system and for the head injury criteria (HIC).

Other crashworthiness references include the U. S. Army Crash Survival Design Guide [11], as well as numerous NASA technical reports. The U. S. Army Crash Survival Design Guide presents experimental data to support the validity of an analysis procedure for determining the total load-deflection characteristics, including failure and post-failure behavior, for a given substructure. This analysis procedure employs a number of simplifying assumptions in the problem formulation to facilitate the use of simple energy methods in the calculations. Carden [9,12] reported a study to assess structural airplane crash data and to correlate it with flight parameters at impact. He concluded that the data is applicable to the assessment of expected loads at the seat/occupant structural interface for general aviation airplanes during serious but potentially survivable crashes.

The AGATE Advanced Crashworthiness Group concluded, at an early point in the program, that a significant increase in crashworthy performance could only be achieved by employing a systems approach when designing the crashworthy features for the AGATE aircraft. The systems approach is necessary to accurately reflect the large number of interactions that occur between the airframe, the occupants, and the seat and restraint systems. The benefits of this approach include the fact that it provides for a balanced design approach, which considers a range of injury-causing mechanisms, as well as realistic full-scale crash conditions. The AGATE design effort addressed the first four of the five crashworthiness principals listed below.

1. Container - maintain a survivable volume throughout the crash event;
2. Restraint - a restraint system, seats and attachments that are designed to restrain the occupants inside the survivable volume;
3. Environment - eliminate injury-causing mechanisms in the occupants' environment;
4. Energy Management - limit the occupant loads and accelerations to tolerable levels (considering seats, restraints, fuselage, engine mounts, etc.); and
5. Post-crash Factors - fuel system and egress.

The systems approach inherently enables the vehicle to be designed to impact conditions that are much more severe than those specified in the FAA dynamic seat certification requirements. This observation is true by virtue of the fact that the AGATE design integration effort involves all, rather than a subset, of the relevant vehicle systems.

THIS DOCUMENT PROVIDED BY THE ABBOTT AEROSPACE
TECHNICAL LIBRARY
ABBOTTAEROSPACE.COM

The safety technologies incorporated in the AGATE airplane design are shown in Figure 1. These include a very stiff, strong cabin to provide a protective shell for the occupants and an energy absorbing engine mount to control the aircraft response during soft soil impacts. It also includes an energy absorbing subfloor and crashworthy seats to attenuate spinal loads. Advanced restraints and energy absorbing seats represent the final elements in the occupant protection system.

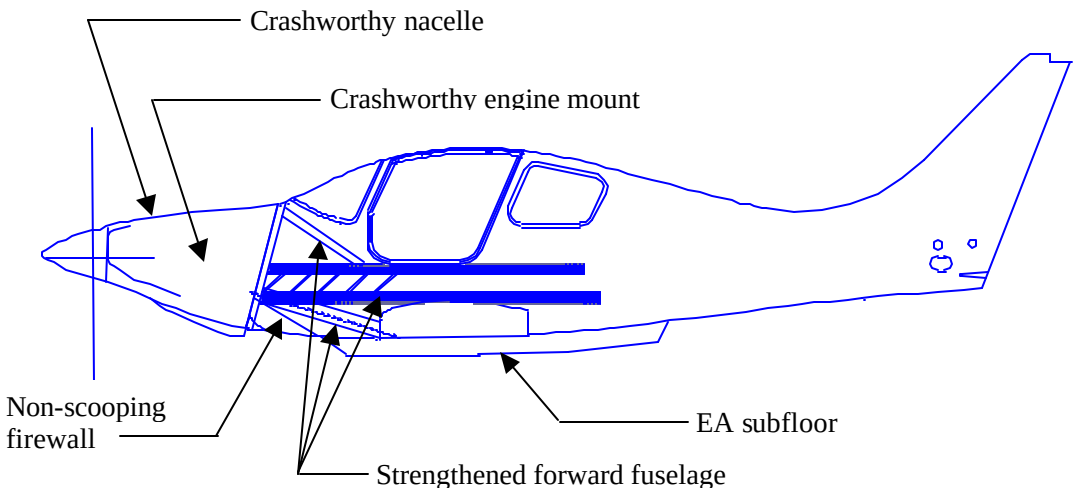

Figure 1. AGATE Safety Technologies

The success of these technologies depends on their performance as well as the manufacturing and certification costs. The AGATE team agreed that a simple, but conservative approach to the crashworthiness design problem, is preferable to a complicated one. Therefore, they sought a crashworthiness load definition that can be used to design the cabin structure as a static load condition in the same way that flight and maneuver loads are traditionally used to design the airframe. Such an approach can be readily implemented since it represents an extension of the current engineering practices, and as such, requires no new skills.

Many pre-1990 general aviation designs tested at NASA Langley Research Center did not perform very well in soft soil crash tests [6,13]. These airframes frequently exhibited very high longitudinal decelerations that were either associated with forward fuselage loads of such a magnitude that they compromised the survivable volume or they defeated the occupant protection systems (seats and restraints). In many cases the source of these high loads is the momentum transfer produced as the aircraft displaces soil during the impact event. Terry [1] reported that approximately 560 lb. of soil was ejected from the crater in his first soft soil test and 390 lb. of soil in his second soil test. This material was distributed up to 300 ft. downrange from the impact point.

Terry studied the behavior of a general aviation aircraft impacting a soft soil surface and concluded that a crashworthy GA aircraft must be designed to "ride-up" on the soil much like a ski glides over snow. He also identified the engine mount and lower cowl structure as two important components in a crashworthy system that must be designed to attenuate the airframe acceleration during this response. He also restated the necessity of designing the lower firewall in a manner that does not scoop soil. This feature was clearly described in the U.S Army Crash Survival Design Guide [11], but was generally not reflected in many of pre-1990 general aviation designs.

THIS DOCUMENT PROVIDED BY THE ABBOTT AEROSPACE
TECHNICAL LIBRARY
ABBOTTAEROSPACE.COM

The importance of a non-scooping design is easily explained in terms of fundamental impulse-momentum theory. The familiar impulse-momentum equation is written as

$$\int_{t_1}^{t_2} F(t)\,dt = mV_2 - mV_1$$

When applying this equation, it is important to recognize that the total velocity change $V_2 - V_1$ is a function of the crash conditions, not the airplane design. Also recall that it is necessary to attenuate the forces $F(t)$ to levels tolerable to the occupants. Clearly, this becomes more likely as the stopping time t_2 - t_1 increases and it is this, which is precisely the function of the engine mount / cowl / lower firewall system. It is of fundamental importance to recognize that the occupant protection is significantly enhanced by designing the vehicle to maximize the vehicle's stopping time. In many good designs this is achieved without employing any energy absorbing structures.

The engine mount / cowl / lower firewall system is also critical in managing the vertical component of the momentum change since it is this structure that makes first contact with the ground. Thus it is this same structure that must appropriately resist the contact forces and produce the pitching moments that rotate the aircraft's velocity vector to a direction parallel to the ground. The deformation characteristics of the engine mount are very important in producing the desired airframe response and may, as in the case of the Terry designs, involve nonconservative energy absorbing mechanisms.

This report describes a method for extracting impact loads from full-scale drop test data. Crashworthy engine mount loads are extracted from data acquired during a full-scale airplane drop test as the first step in this method. These loads will be used in the preliminary sizing of the fuselage structure just aft of the firewall. This structure is critical to the crashworthy performance of a general aviation aircraft since it is the highest-loaded portion of the cabin structure that must be designed to maintain a survivable volume during the crash event. These loads could be verified by comparing them to predictions developed using nonlinear finite element models in the validation of these analyses.

The nose of an aircraft is the first thing to contact the ground in many aircraft accidents, especially those that occur as a consequence of a stall or spin at low altitude. The contact forces produced during these impacts are needed to calculate a rigid body aircraft response and its structural response to the accident load condition. This report documents a simple method to extract these loads from the drop test data of an AGATE-class aircraft [1,2]. The approach utilizes acceleration data measured at specific points along the fuselage as well as a number of simplifying assumptions to calculate the longitudinal and vertical impact forces, the angular acceleration of the aircraft at impact, and the firewall loads.

THIS DOCUMENT PROVIDED BY THE ABBOTT AEROSPACE
TECHNICAL LIBRARY
ABBOTTAEROSPACE.COM

The AGATE Crashworthiness Group defined a 30° nose-down impact at $\mathbf{V_{so}}$ as the AGATE crash condition where the aircraft's longitudinal axis is aligned with the flight path as shown in Figure 2.

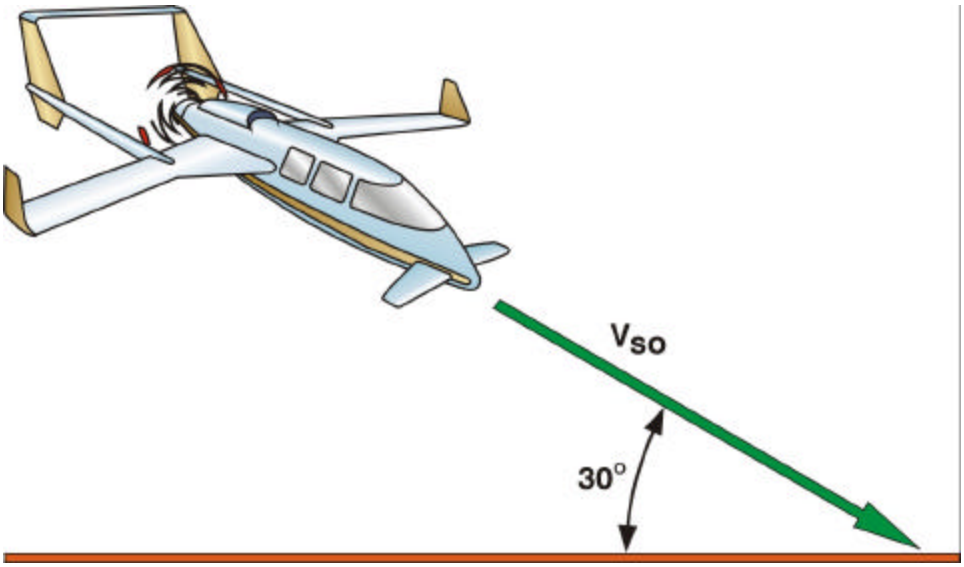

Figure 2. Drop Test Conditions

The data reported by Terry [1] are utilized in the following analysis. This program involved four full-scale drop tests of a composite general aviation aircraft that were designed to crash conditions that are very similar to the ones identified during the AGATE program. Two of these drop tests were onto a hard surface, and two were into soft soil.

THIS DOCUMENT PROVIDED BY THE ABBOTT AEROSPACE
TECHNICAL LIBRARY
ABBOTTAEROSPACE.COM

The whole-aircraft drop test articles utilized for these drop tests included a number of added AGATE safety features as shown in Figure 3. The engine mount design is particularly relevant to the analysis presented in this report, which is based on a modified version of Carden's free body diagram [9,12] shown in Figure 4. Since the aircraft is treated as a rigid body, the deformation of the structure is neglected. The aerodynamic forces are also neglected and the yaw and roll angles are assumed to be zero.

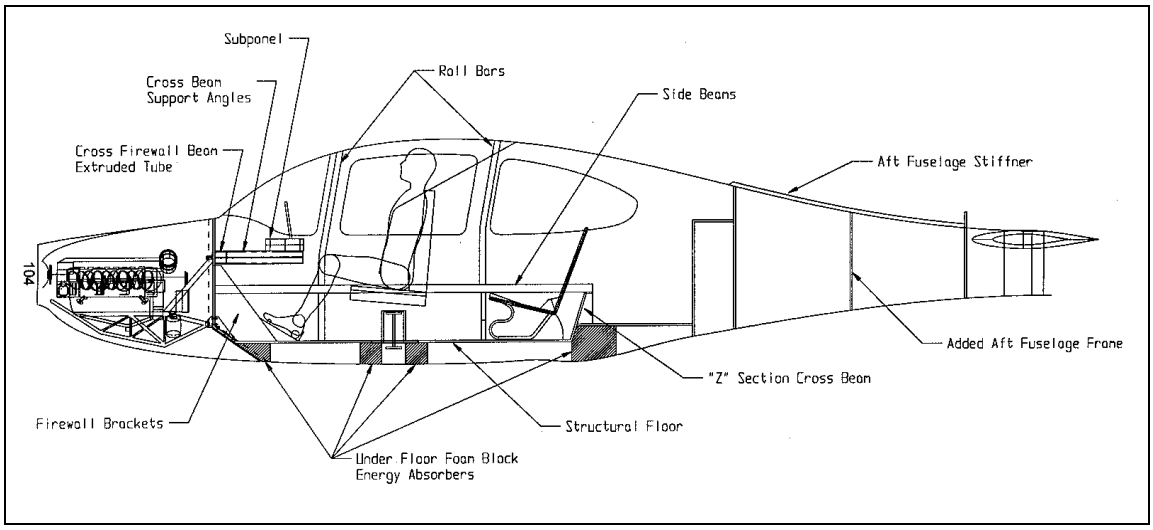

Figure 3. Terry Safety Features

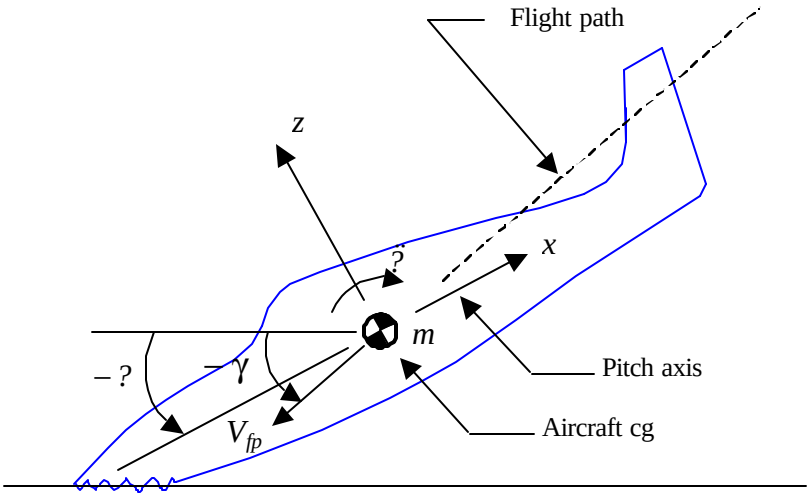

Figure 4. Simplified Crash Idealization

THIS DOCUMENT PROVIDED BY THE ABBOTT AEROSPACE
TECHNICAL LIBRARY
ABBOTTAEROSPACE.COM

Drop Test Data Analysis

The firewall loads are developed from an analysis of Terry's "Full Scale Test 2, Soft Soil" (Test 2) and "Full Scale Test 3, Soft Soil" (Test 3) data. The drop test conditions for these tests are summarized in Table 1, utilizing the terminology presented in Figure 4.

Table 1. Drop test conditions

	Test 2	Test 3	
Aircraft weight	2500 lb.	2500 lb.	
Impact velocity	84 ft/sec	82.3 ft/sec	V_{fp}
Flight path angle	-30 degrees	-30 degrees	γ
Aircraft Attitude (pitch angle)	-27.2 degrees	-23.5 degrees	θ
Average airfield index	2.8 (at a depth of 10")	3.4 (at a depth of 10")	

The aircraft drop test articles were instrumented with accelerometers and load cells as shown in Figure 5.

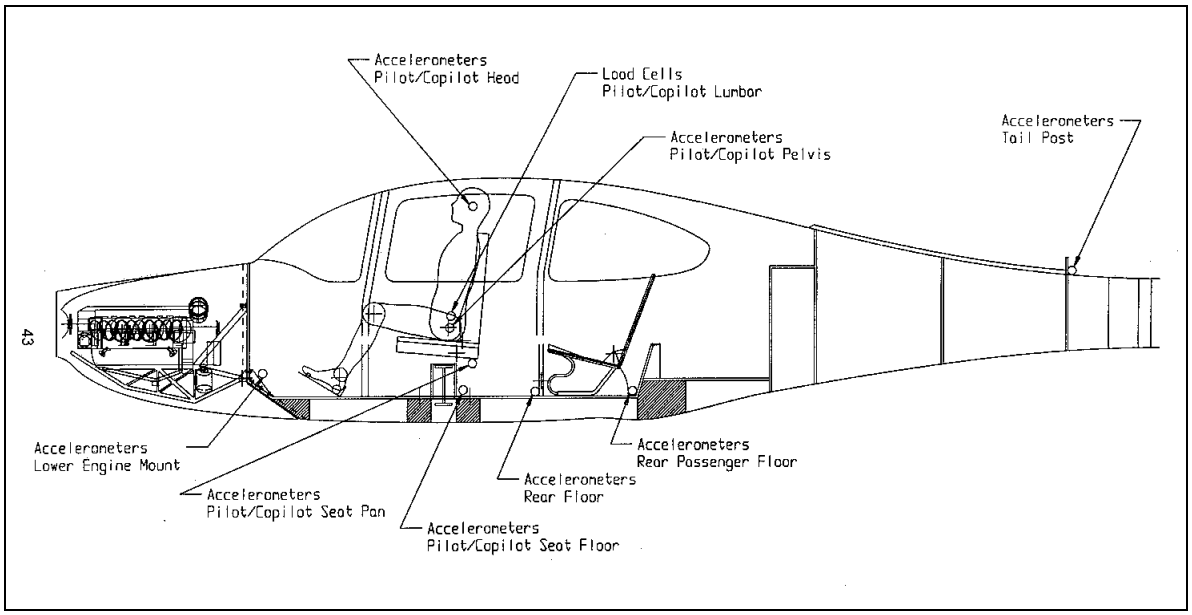

Figure 5. Drop Test Instrumentation

The analysis, described in this report, utilized the following data:

1. "Accelerometers Lower Engine Mount" (left and right)
2. "Accelerometers Pilot/Copilot Seat Floor" (pilot and copilot)
3. "Accelerometers Rear Floor" (one location)

The test conditions, i.e. impact attitude, velocity, and impact surface, were very similar for Tests 2 and 3. However, different engine mount designs were used and the data reflects the differences in their responses. The airframe responses during these tests are presented in Figures 6 and 7.

This Document Provided by the Abbott Aerospace
TECHNICAL LIBRARY
ABBOTTAEROSPACE.COM


Impact


t = .020 seconds

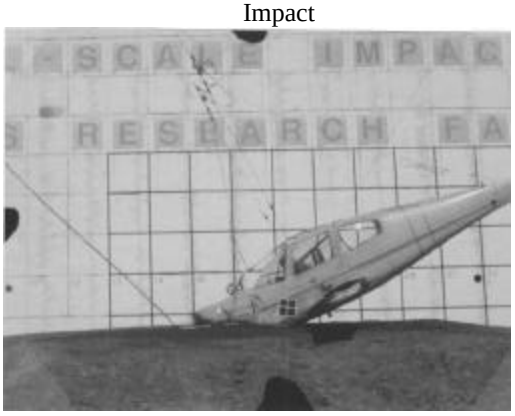
t = .040 seconds


t = .060 seconds


t = .080 seconds


t = .100 seconds


t = .120 seconds


t = .140 seconds

Figure 6. Crash Sequence Photographs for Test 2 [1]

THIS DOCUMENT PROVIDED BY THE ABBOTT AEROSPACE
TECHNICAL LIBRARY
ABBOTTAEROSPACE.COM


Impact


t = .020 seconds


t = .040 seconds


t = .060 seconds


t = .080 seconds


t = .100 seconds


t = .120 seconds


t = .140 seconds

Figure 7. Crash Sequence Photographs for Test 3 [1]

THIS DOCUMENT PROVIDED BY THE ABBOTT AEROSPACE
TECHNICAL LIBRARY
ABBOTTAEROSPACE.COM

The lower engine mount longitudinal acceleration data were utilized to calculate a force time-history. The acceleration time-history curves, in the x direction, for the left lower and right lower engine mounts are presented in Figures 9 and 11. These data were obtained from graphs presented in Ref. 1, digitized, and then filtered. The three curves shown below include the digitized data curve (yellow) and the filtered data curve (red) with the corresponding Terry data curve (black). The reader should note that this presentation format has been used throughout this report. Simplified curves, presented in Figures 10 and 12, were defined and will subsequently be used to estimate the acceleration data.

A comparison of the filtered and unfiltered data in this, and all subsequent cases points to the observation that mechanisms associated with local deformations often produce oscillatory load-deflection curves and high-frequency responses in the time domain. Extremely low SAE channel filter classes (SAE CFC) are required to suppress these signals. This technique may not be desirable or appropriate since it may produce inaccurate and misleading results.

Consequently, the authors elected to smooth Terry's crash test data using the approach reported by Carden [9,12]. This technique presumes the presence of three components to the measured response, as defined in Appendix A, including: 1. The primary structural response, 2. The secondary structural response associated with local deformations, and 3. Noise. Considering compressively loaded structures, examples of primary responses include column buckling and panel buckling while examples of secondary responses include mechanisms like the crippling of columns or wrinkling of sandwich panel face sheets. While the use of SAE CFC filtering is appropriate for removing noise, its use is questionable and probably inappropriate for distinguishing between the primary and secondary structural responses.

The secondary structural response associated with local deformations can be illustrated by examining the post-crash engine mount from Terry's Test 2 (Figure 8). The resulting oscillatory force-time history contains a primary and a secondary response as discussed in Appendix A. The subsequent analysis only considers the primary response.

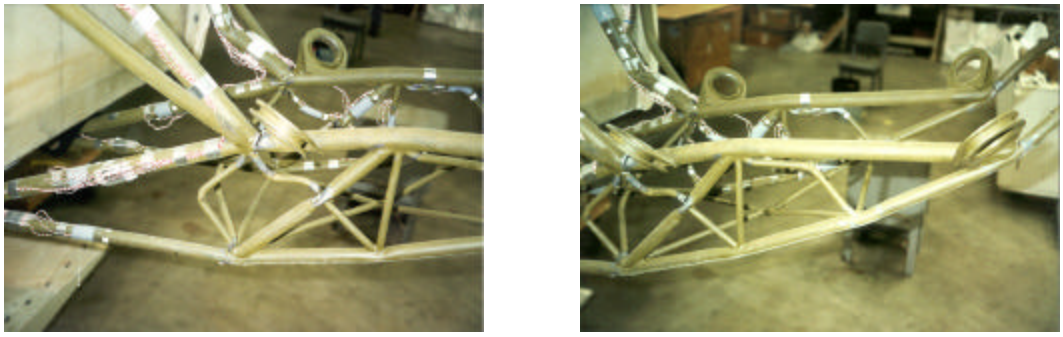

Figure 8. Test 2 Post-Crash Engine Mount

THIS DOCUMENT PROVIDED BY THE ABBOTT AEROSPACE
TECHNICAL LIBRARY
ABBOTTAEROSPACE.COM

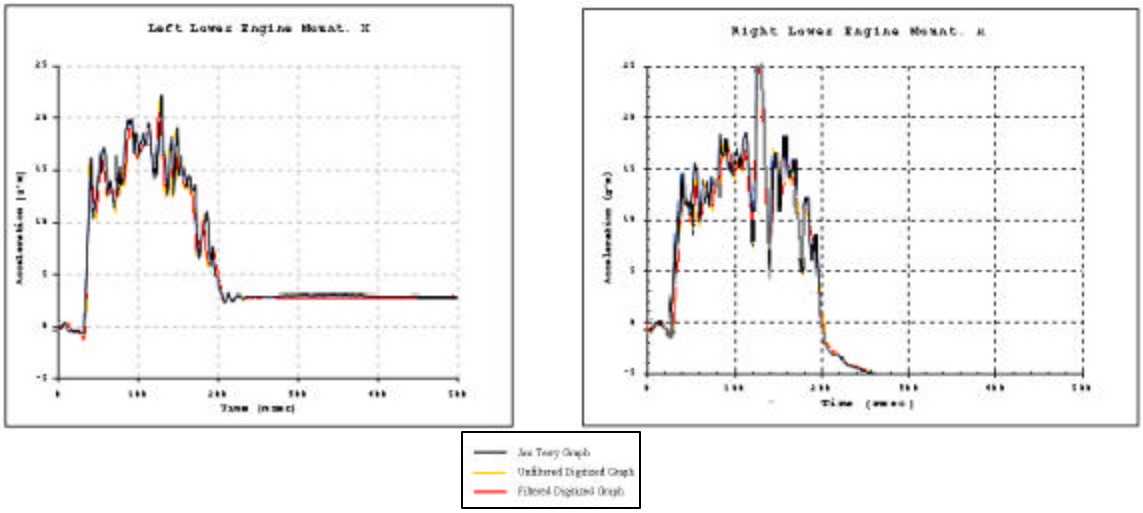

Figure 9. Test 2 Drop Test Engine Mount Acceleration Data (ẍ) [1]

The filtered data for the left and right lower engine mounts are presented in the left graph in Figure 10 along with a simplified representation of these data, which is presented again for clarity in the graph on the right side of the figure. The simplified curve is somewhat arbitrary and is defined using engineering judgment. Carden [9,12] employed a similar technique in the analysis of early full-scale drop test data.

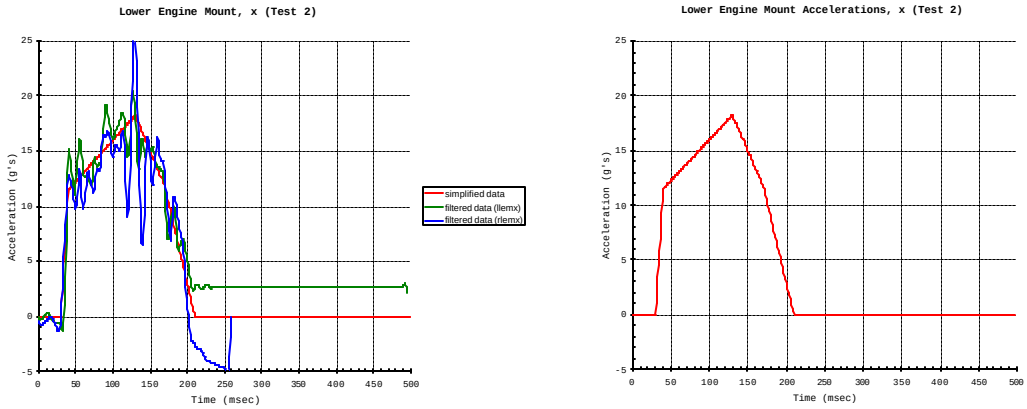

Figure 10. Test 2 Lower Engine Mount Accelerations (ẍ)

THIS DOCUMENT PROVIDED BY THE ABBOTT AEROSPACE
TECHNICAL LIBRARY
ABBOTTAEROSPACE.COM

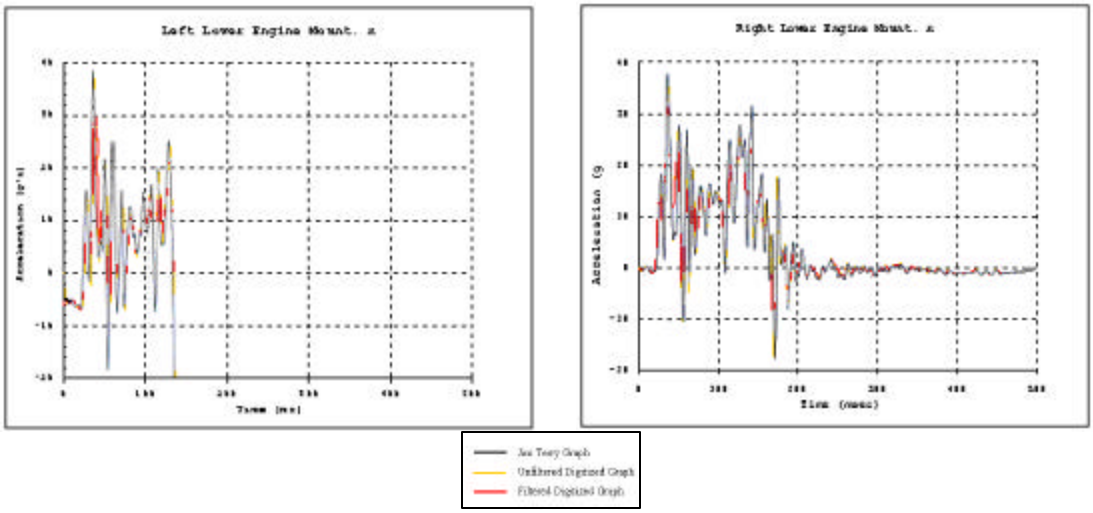

Figure 11. Test 3 Drop Test Engine Mount Acceleration Data ($\ddot{x}$) [1]

As before, the graph on the left side of Figure 12 contains the filtered data for the lower engine mounts as well as the idealized curve, which is presented again for clarity in the graph on the right hand side of Figure 12.

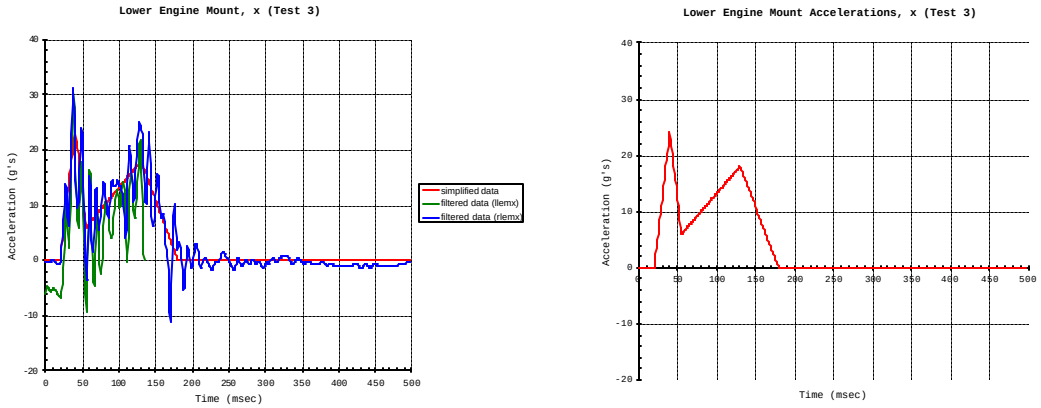

Figure 12. Test 3 Lower Engine Mount Accelerations ($\ddot{x}$)

THIS DOCUMENT PROVIDED BY THE ABBOTT AEROSPACE
TECHNICAL LIBRARY
ABBOTTAEROSPACE.COM

The longitudinal accelerations at the center of gravity (cg) of the airplane are needed in order to calculate the longitudinal force time-history. The accelerometers located at the pilot and copilot seat floor were near the aircraft cg. However, the longitudinal acceleration data from the pilot seat floor and the copilot seat floor appears to be incomplete. A comparison of the initial lower engine mount acceleration data with that acquired at pilot floor locations reveals little difference, therefore the longitudinal accelerations at the cg are assumed to be the same as the rigid body longitudinal accelerations at the lower engine mount locations.

The resulting force time-histories are shown in Figures 13 and 14. These were calculated using Newton's 2nd Law,

$$\sum F_x = m\ddot{x} \tag{1}$$

considering the mass of the aircraft to be 2500 lb/g.

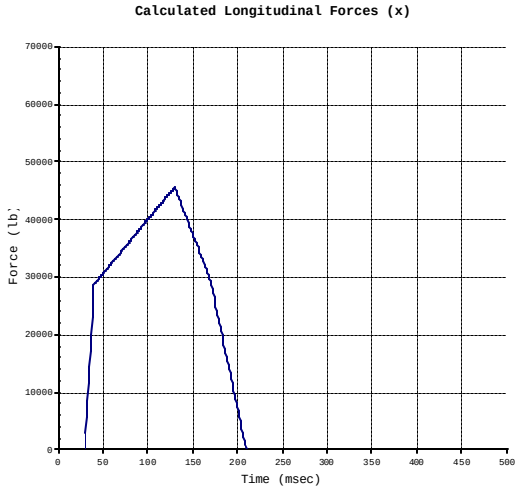

Figure 13. Test 2 Force Time-History (longitudinal impact)

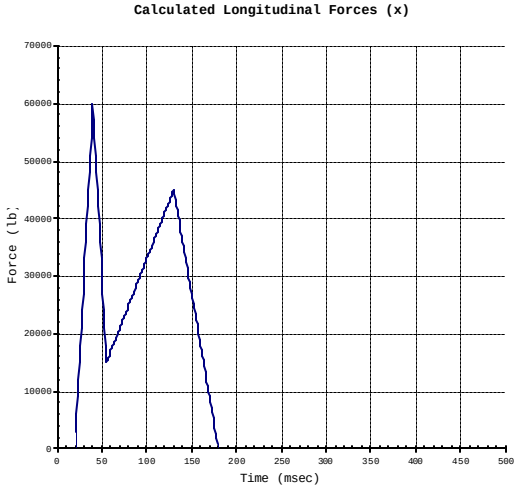

Figure 14. Test 3 Force Time-History (longitudinal impact)

THIS DOCUMENT PROVIDED BY THE ABBOTT AEROSPACE
TECHNICAL LIBRARY
ABBOTTAEROSPACE.COM

A similar analysis was employed to generate the force time-histories in the z (vertical) direction. The acceleration time-history curves, in the z direction, for the left lower and right lower engine mounts are presented in Figures 15 and 17. The corresponding simplified curves are presented in Figures 16 and 18.

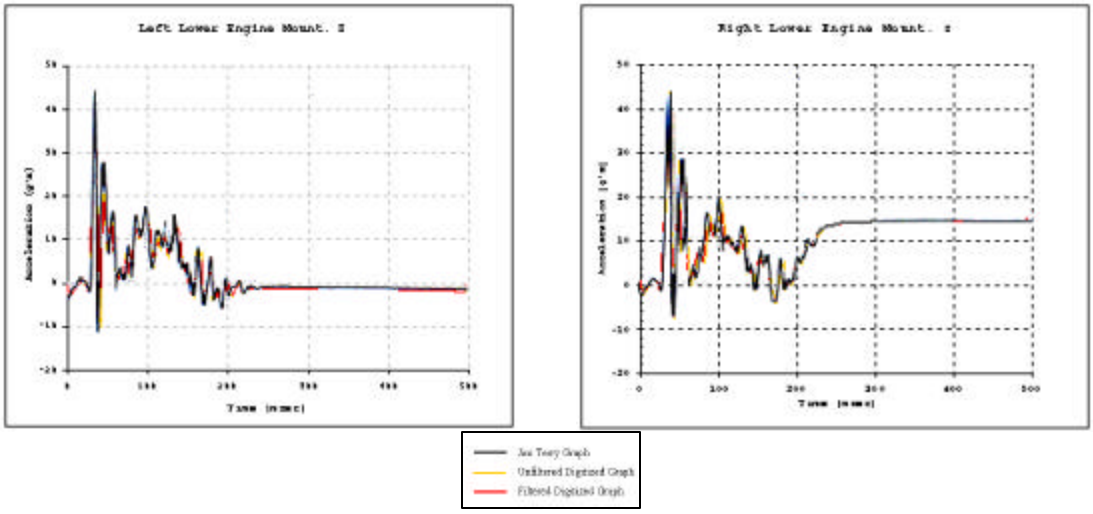

Figure 15. Test 2 Drop Test Engine Mount Acceleration Data (ẗ) [1]

The graph on the left side of Figure 16 contains the filtered data for the lower engine mounts as well as the idealized curve, which is presented again for clarity in the graph on the right hand side of Figure 16.

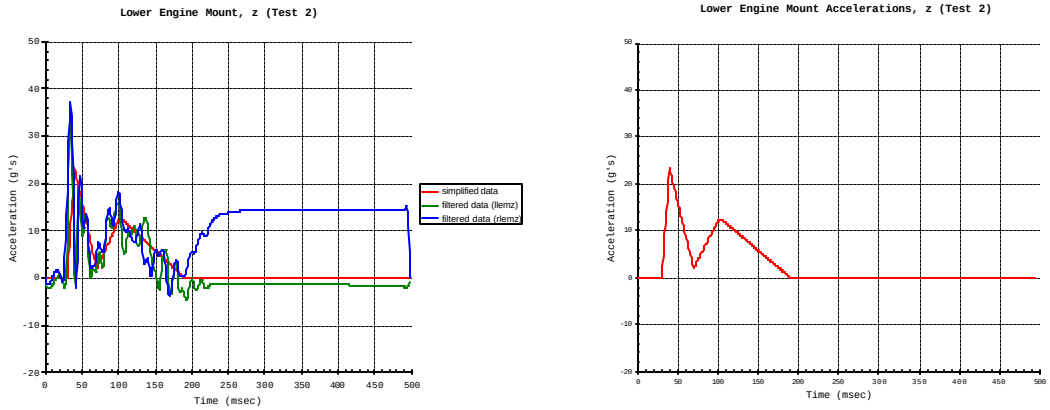

Figure 16. Test 2 Lower Engine Mount Accelerations (ẗ)

THIS DOCUMENT PROVIDED BY THE ABBOTT AEROSPACE
TECHNICAL LIBRARY
ABBOTTAEROSPACE.COM

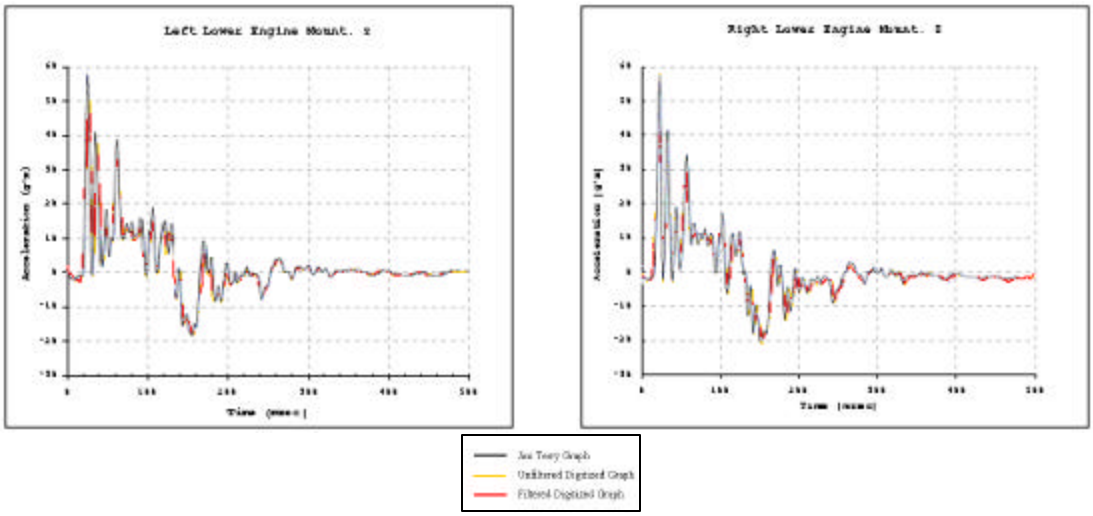

Figure 17. Test 3 Drop Test Engine Mount Acceleration Data (ẗ) [1]

As before, the graph on the left side of Figure 18 contains the filtered data for the lower engine mounts as well as the idealized curve, which is presented again for clarity in the graph on the right hand side of Figure 18.

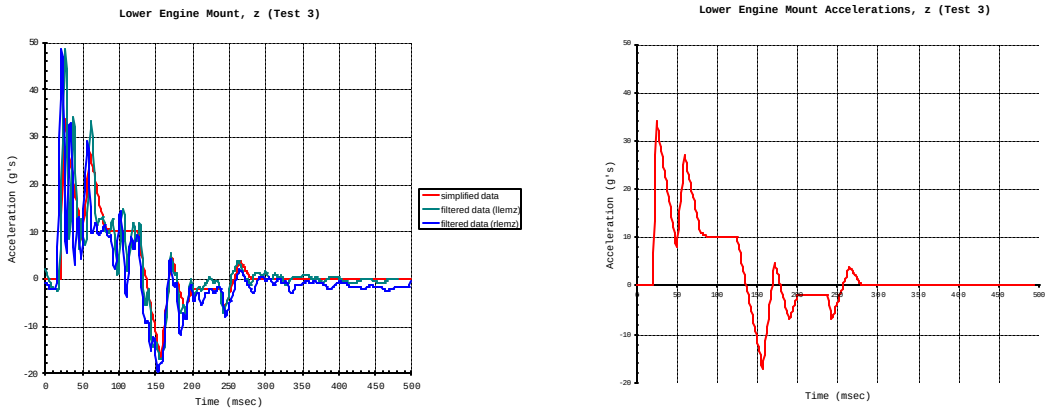

Figure 18. Test 3 Lower Engine Mount Accelerations (ẗ)

THIS DOCUMENT PROVIDED BY THE ABBOTT AEROSPACE
TECHNICAL LIBRARY
ABBOTTAEROSPACE.COM

The acceleration time-history curves, in the z direction, at the pilot and copilot seat floor locations are presented in Figures 19 and 21. The corresponding simplified curves are shown in Figures 20 and 22.

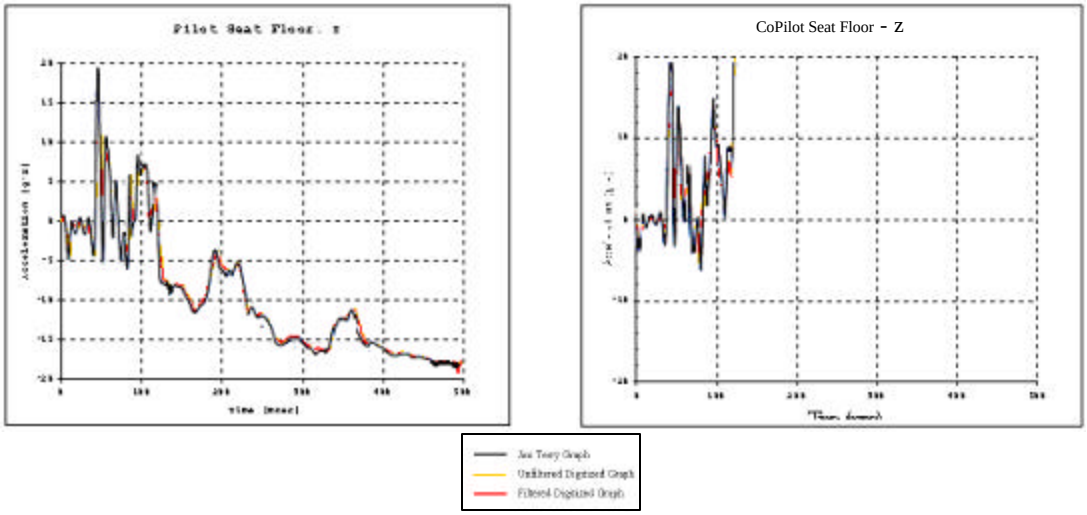

Figure 19. Test 2 Drop Test Pilot/Copilot Seat Floor Acceleration Data (z̈) [1]

The graph on the left side of Figure 20 contains the filtered data for the pilot and copilot seat floor as well as the idealized curve, which is presented again for clarity in the graph on the right hand side of Figure 20.

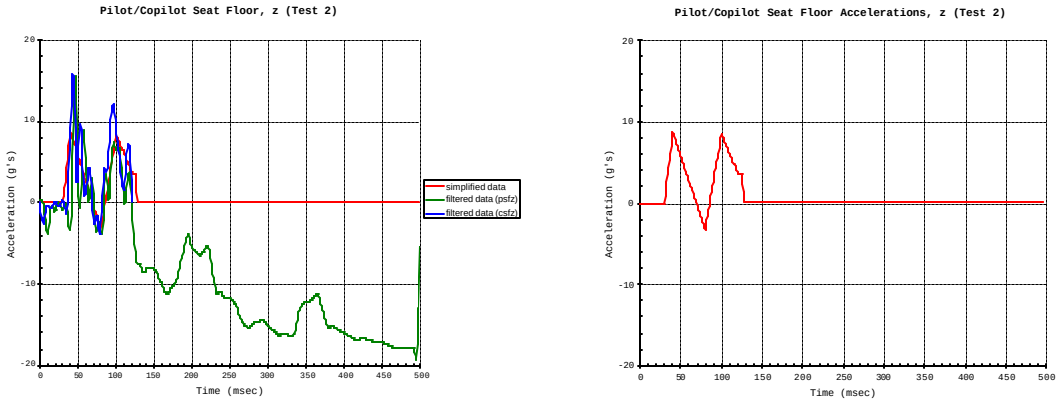

Figure 20. Test 2 Pilot/Copi lot Seat Floor Accelerations (z̈)

THIS DOCUMENT PROVIDED BY THE ABBOTT AEROSPACE
TECHNICAL LIBRARY
ABBOTTAEROSPACE.COM

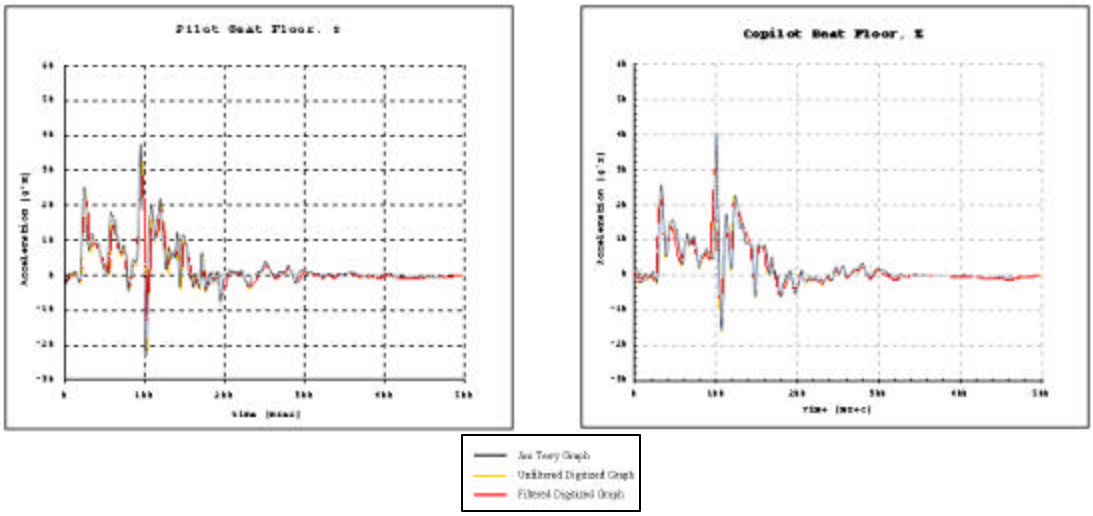

Figure 21. Test 3 Drop Test Pilot/Copilot Seat Floor Acceleration Data (z̈) [1]

As before, the graph on the left side of Figure 22 contains the filtered data for the pilot and copilot seat floor as well as the idealized curve, which is presented again for clarity in the graph on the right hand side of Figure 22.

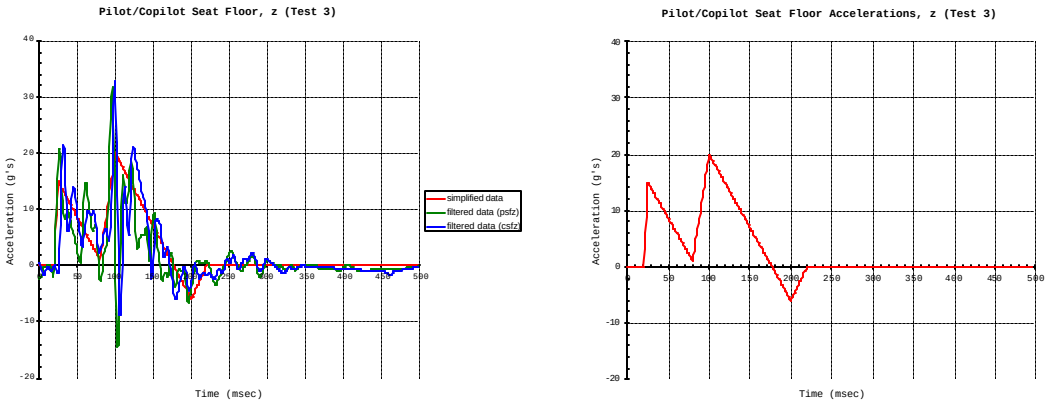

Figure 22. Test 3 Pilot/Copilot Seat Floor Accelerations (z̈)

THIS DOCUMENT PROVIDED BY THE ABBOTT AEROSPACE
TECHNICAL LIBRARY
ABBOTTAEROSPACE.COM

The z-acceleration time-history curves for the rear floor location are presented in Figures 23 and 25. The corresponding simplified curves are shown in Figures 24 and 26.

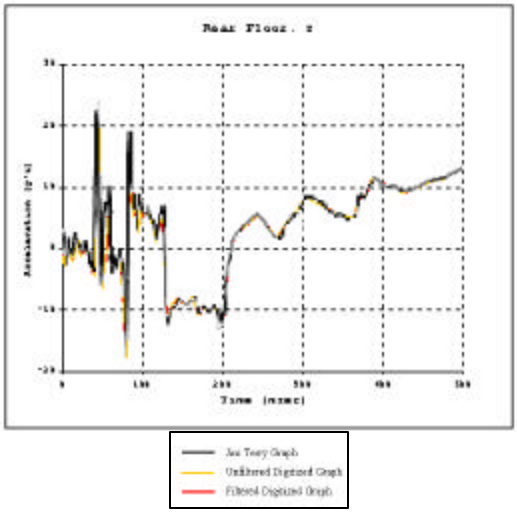

Figure 23. Test 2 Drop Test Rear Floor Acceleration Data (ẗ) [1]

The graph on the left side of Figure 24 contains the filtered data for the rear floor as well as the idealized curve, which is presented again for clarity in the graph on the right hand side of Figure 24.

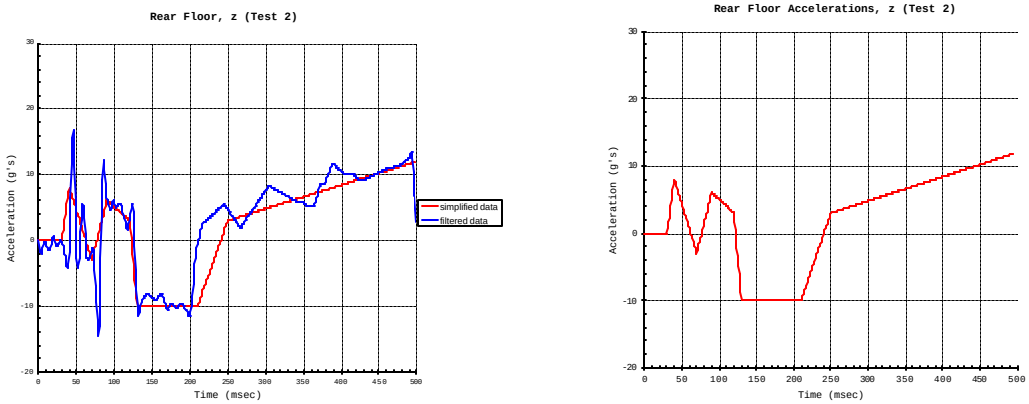

Figure 24. Test 2 Rear Floor Accelerations (ẗ)

THIS DOCUMENT PROVIDED BY THE ABBOTT AEROSPACE
TECHNICAL LIBRARY
ABBOTTAEROSPACE.COM

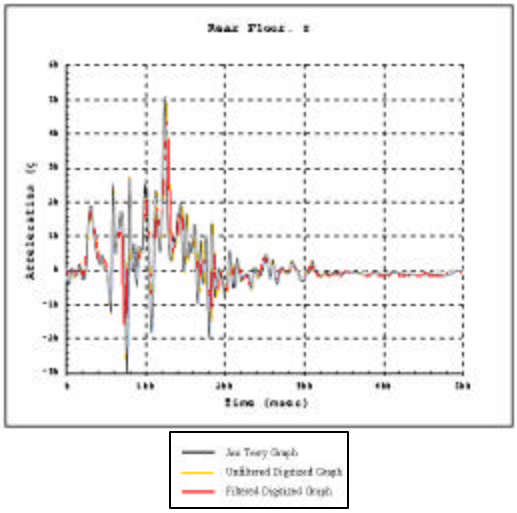

Figure 25. Test 3 Drop Test Rear Floor Acceleration Data (ẗ) [1]

As before, the graph on the left side of Figure 26 contains the filtered data for the rear floor as well as the idealized curve, which is presented again for clarity in the graph on the right hand side of Figure 26.

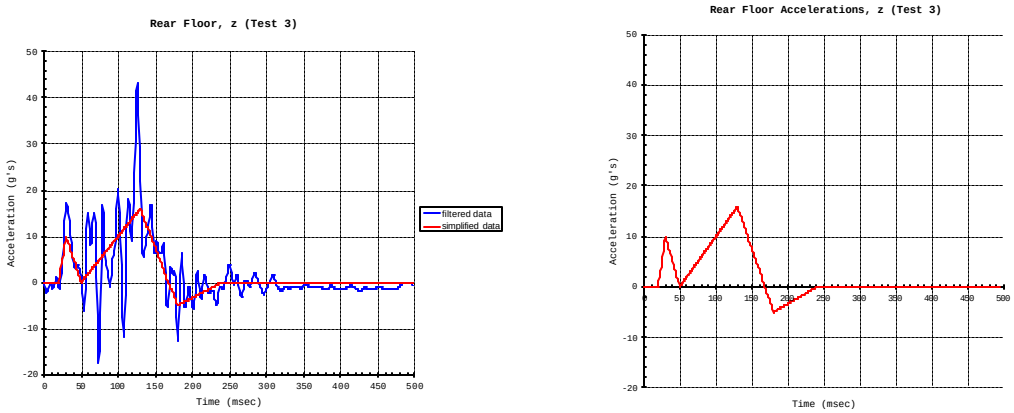

Figure 26. Test 3 Rear Floor Accelerations (ẗ)

THIS DOCUMENT PROVIDED BY THE ABBOTT AEROSPACE
TECHNICAL LIBRARY
ABBOTTAEROSPACE.COM

Figures 16, 18, 20, 22, 24, and 26 present vertical acceleration data at 3 different fuselage stations at locations shown in Figure 27. The distances between the accelerometers were estimated by scaling the fuselage drawing reported in Reference 1.

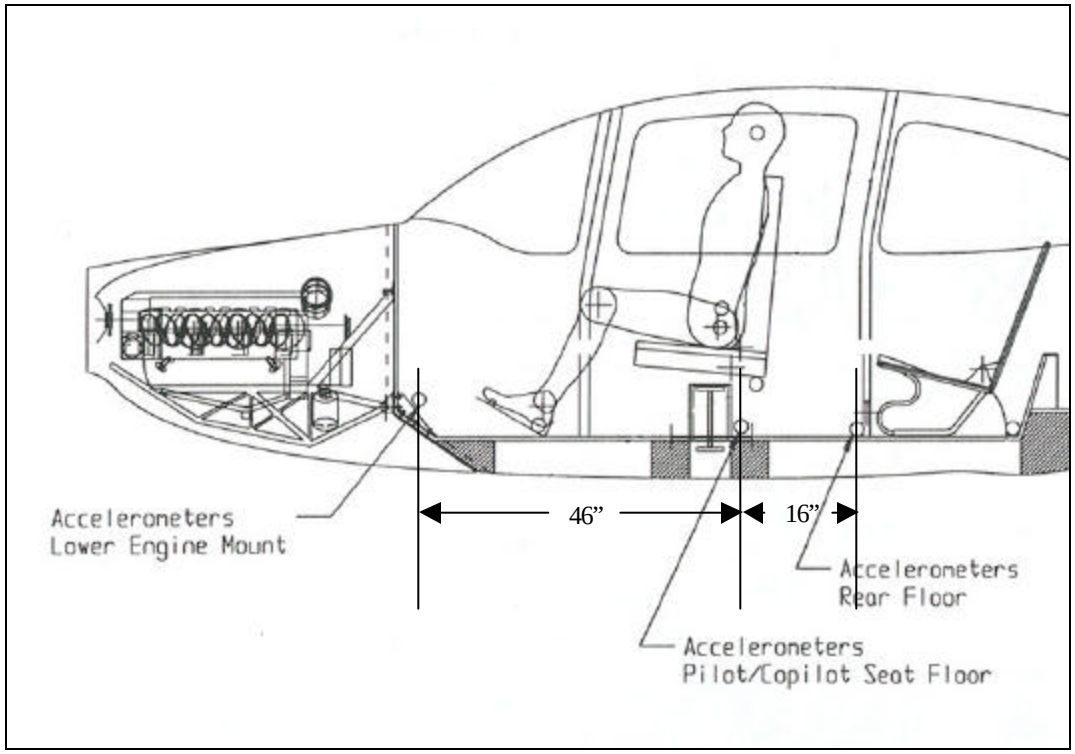

Figure 27. Drop Test Instrumentation Distances

THIS DOCUMENT PROVIDED BY THE ABBOTT AEROSPACE
TECHNICAL LIBRARY
ABBOTTAEROSPACE.COM

As discussed earlier, it is assumed that the pilot/copilot seat floor accelerometer positions represent the longitudinal location of the aircraft cg. The vertical acceleration data from the 3 locations shown in Figure 27 were analyzed by the method of least squares, fitting a straight line through the 3 acceleration values, and then extracting an acceleration value from the line at the assumed cg location. These resulting vertical acceleration data at the cg are shown in Figures 28 and 29.

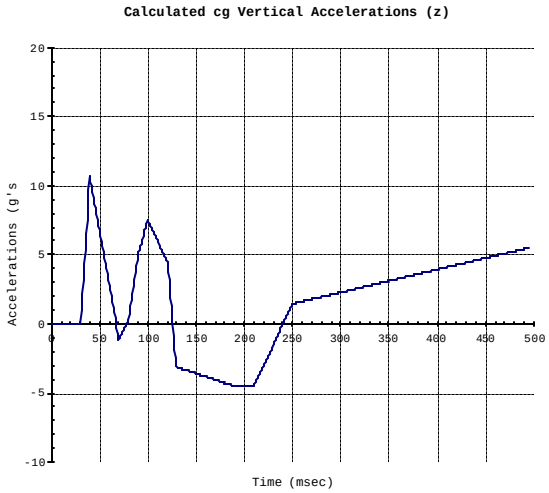

Figure 28. Test 2 Vertical Accelerations at Airplane Center of Gravity ($\ddot{z}$)

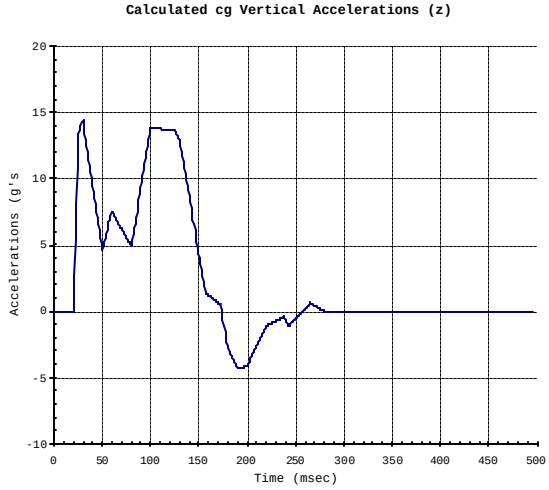

Figure 29. Test 3 Vertical Accelerations at Airplane Center of Gravity ($\ddot{z}$)

THIS DOCUMENT PROVIDED BY THE ABBOTT AEROSPACE
TECHNICAL LIBRARY
ABBOTTAEROSPACE.COM

The corresponding force time-histories are shown in Figures 30 and 31. These were calculated using the data shown in Figures 28 and 29 and Newton's 2nd Law

$$\sum F_z = m\ddot{z} \tag{2}$$

again considering the mass of the aircraft to be 2500 lb/g.

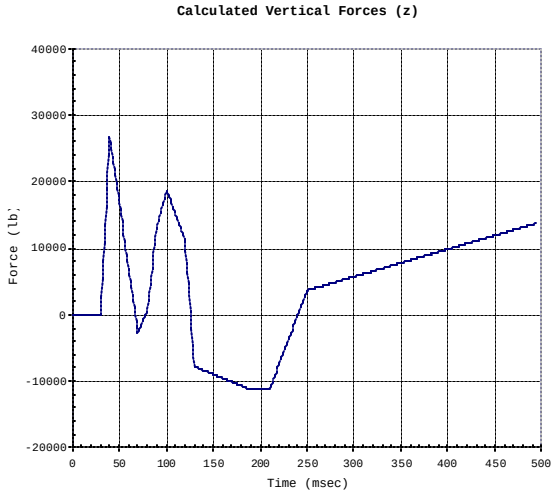

Figure 30. Test 2 Force Time-History (vertical impact)

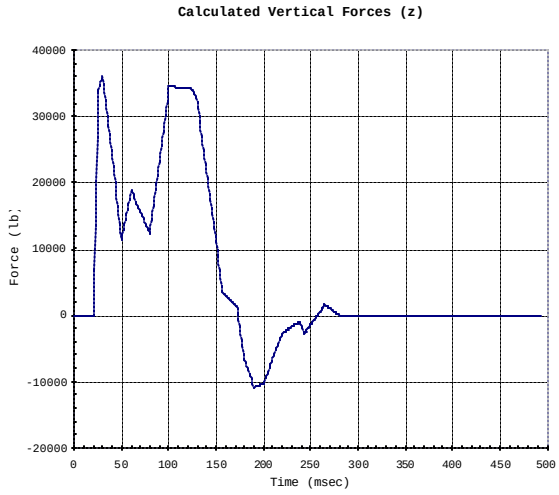

Figure 31. Test 3 Force Time-History (vertical impact)

THIS DOCUMENT PROVIDED BY THE ABBOTT AEROSPACE
TECHNICAL LIBRARY
ABBOTTAEROSPACE.COM

The pitching acceleration of the airplane, $\ddot{\theta}$, was calculated using a procedure similar to that employed to analyze the acceleration in the z direction. The vertical acceleration data from the 3 locations shown in Figure 27 were analyzed by the method of least squares; the slope of the resulting straight line is the angular acceleration. The results are shown in Figures 32 and 33.

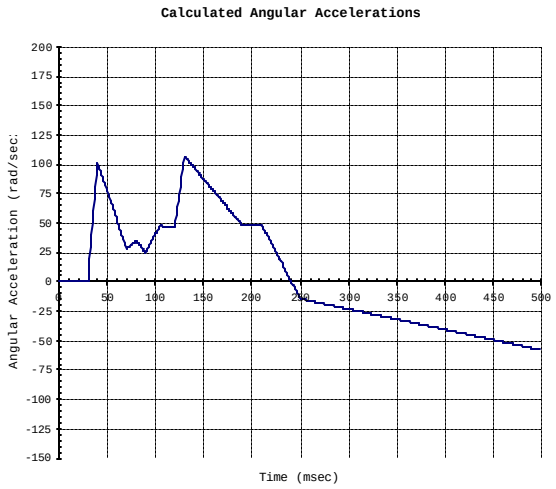

Figure 32. Test 2 Aircraft Pitch Accelerations ($\ddot{\theta}$)

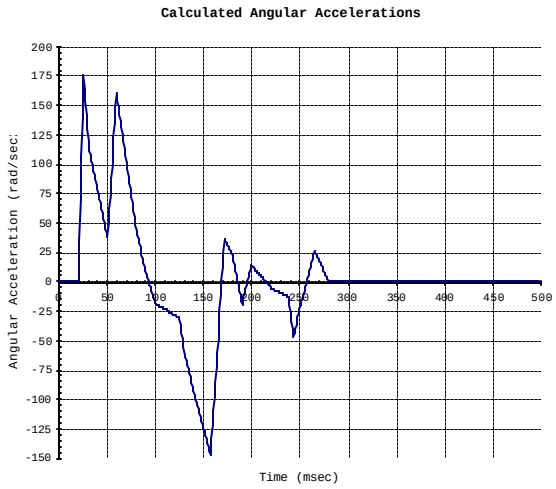

Figure 33. Test 3 Aircraft Pitch Accelerations ($\ddot{\theta}$)

THIS DOCUMENT PROVIDED BY THE ABBOTT AEROSPACE
TECHNICAL LIBRARY
ABBOTTAEROSPACE.COM

The aircraft pitch angles were then calculated using these angular acceleration data. In addition, pitch angles were measured on the still photos of the drop tests presented in Figures 6 and 7. The calculated and measured pitch angles are plotted in Figures 34 and 35.

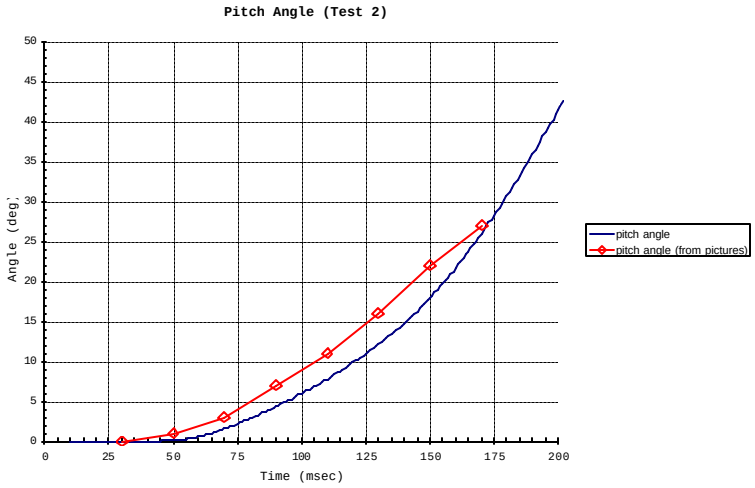

Figure 34. Test 2 Aircraft Pitch Angles (θ)

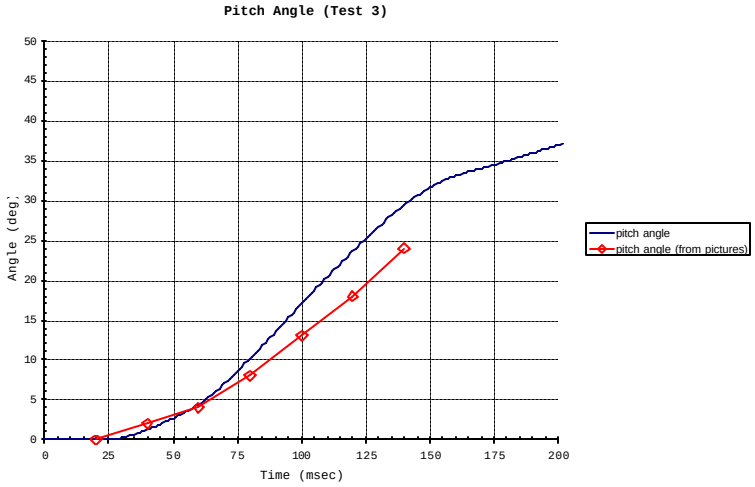

Figure 35. Test 3 Aircraft Pitch Angles (θ)

The measured aircraft pitch angles support the calculated aircraft pitch angle time-history.

THIS DOCUMENT PROVIDED BY THE ABBOTT AEROSPACE
TECHNICAL LIBRARY
ABBOTTAEROSPACE.COM

Firewall Load Estimation

The longitudinal and vertical contact force time-histories, as well as an aircraft pitch acceleration time-history, have been estimated for the first 500 msec of an aircraft impact event, based on the experimental data presented in the previous section of this report. However, the remaining calculations will be made for the first 200 msec of an aircraft impact event.

The longitudinal and vertical contact forces, C_x and C_z, act at a point that is located at distances d_x and d_z from the aircraft center of gravity as shown in Figure 36.

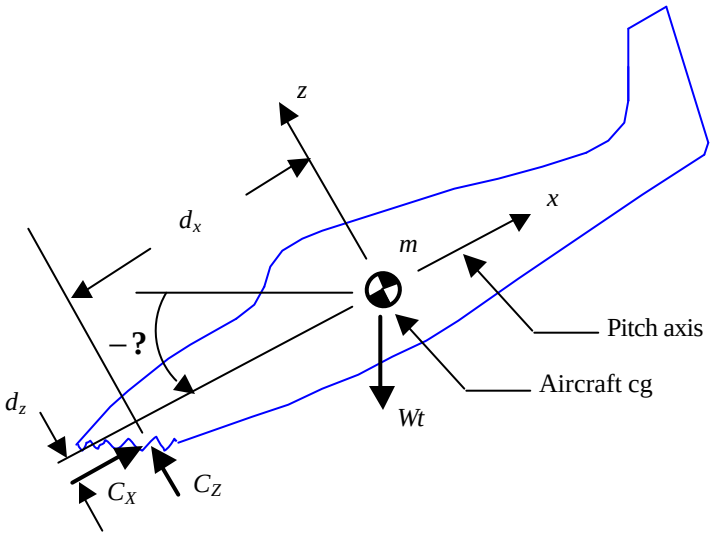

Figure 36. Aircraft Free Body Diagram

The following moment equation can be written based on this free body diagram,

$$\sum M_{cg} = I_{yy}\,\ddot{\theta} = d_x C_z - d_z C_x \qquad (3)$$

and can be solved for the distance d_x. I_{yy} represents the moment of inertia of the aircraft with respect to the y axis about its center of gravity and has been estimated to be 25,000 lb-in^2/g. The distance d_z is assumed to be 24 in.

It is appropriate to examine the force data presented in Figures 30 and 31 before applying this equation. An examination of these figures reveals that the vertical force C_z is greater than zero for most of this time interval. This reflects the three impacts and subsequent rebounds that were recorded during these tests.

THIS DOCUMENT PROVIDED BY THE ABBOTT AEROSPACE
TECHNICAL LIBRARY
ABBOTTAEROSPACE.COM

Substitution of these data into Equation (3) and solving for the moment arm d_x yields singularities in the solution of this equation for values of C_z that are near zero. This is illustrated in Figures 37-40.

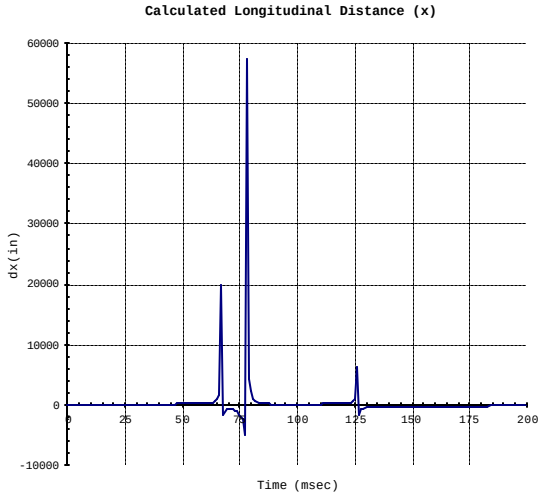

Figure 37. Test 2 Longitudinal Distance Between Aircraft Center of Gravity and Aircraft Impact Point

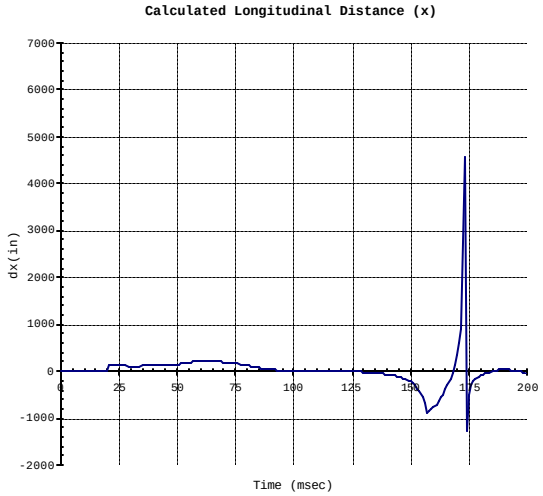

Figure 38. Test 3 Longitudinal Distance Between Aircraft Center of Gravity and Aircraft Impact Point

THIS DOCUMENT PROVIDED BY THE ABBOTT AEROSPACE
TECHNICAL LIBRARY
ABBOTTAEROSPACE.COM

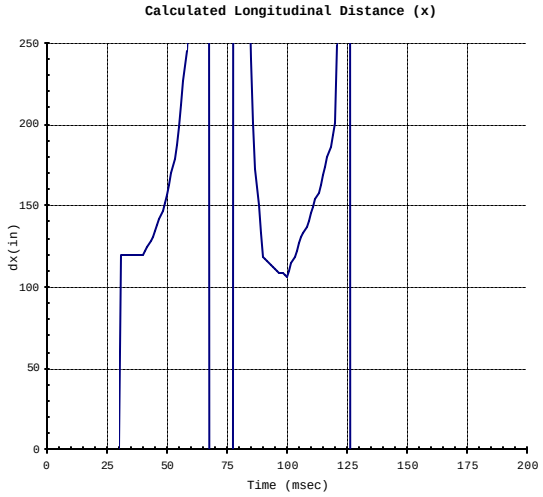

Figure 39. Test 2 Longitudinal Distance Between Aircraft cg and Aircraft Impact Point (smaller scale)

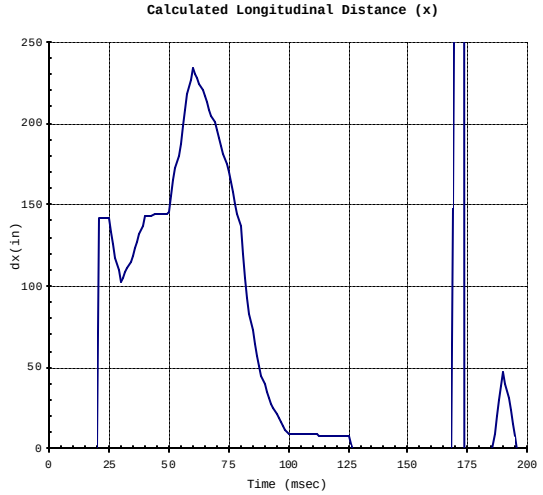

Figure 40. Test 3 Longitudinal Distance Between Aircraft cg and Aircraft Impact Point (smaller scale)

Clearly, the distance d_x cannot take on the extreme values reflected in this solution. The explanation for this behavior is that the moment term $d_x C_z$ vanishes as C_z approaches zero. Thus, the singularities are an artifact of this analysis and possess no physical significance. The values calculated for d_x are valid for the remaining time intervals.

THIS DOCUMENT PROVIDED BY THE ABBOTT AEROSPACE
TECHNICAL LIBRARY
ABBOTTAEROSPACE.COM

Now, consider a free body diagram of the front portion of the aircraft.

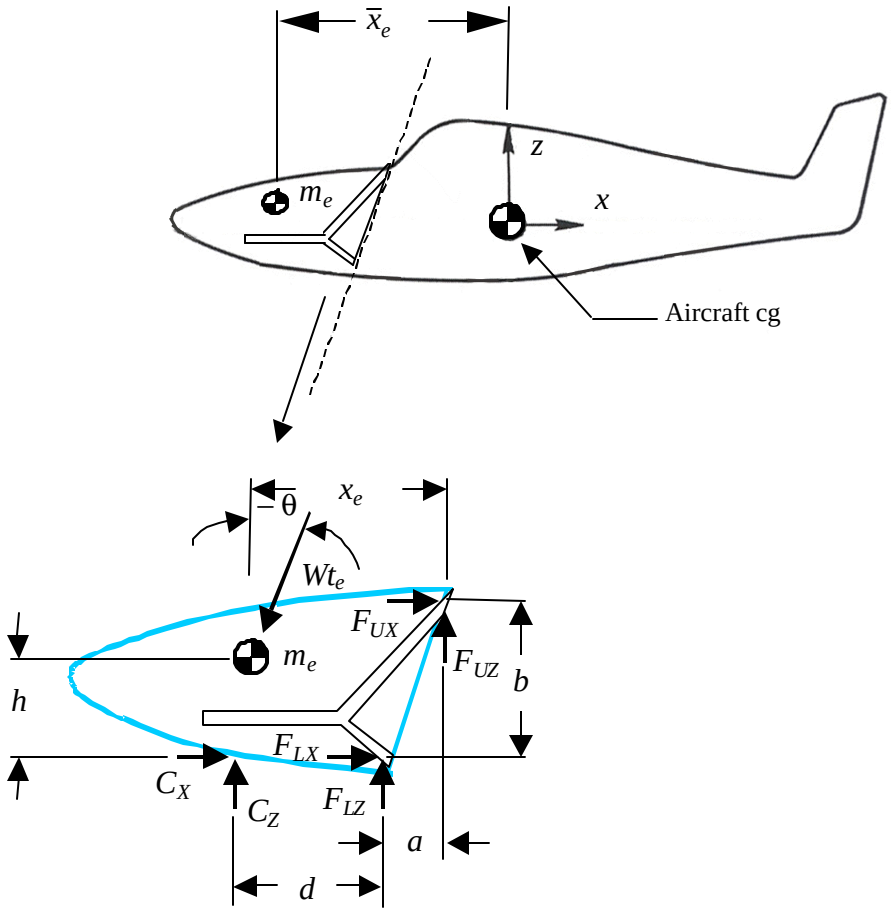

Figure 41. Engine Mount/Nacelle Free-Body Diagram

Considering Figure 41, it is seen that C_x and C_z represent the longitudinal and the vertical impact forces, F_{lx} and F_{lz} represent the longitudinal and the vertical loads at the lower engine mount attachment point, and F_{ux} and F_{uz} represent the longitudinal and the vertical loads at the upper engine mount attachment point. Wt_e and m_e represent the weight of the engine and the mass of the engine, respectively and $\bar{x}_e$ is the longitudinal distance between the aircraft cg and the engine cg. x_e is the longitudinal distance between the upper engine mount attachment and the engine cg. Variables a, b, d, and h define the distances shown in Figure 41.

THIS DOCUMENT PROVIDED BY THE ABBOTT AEROSPACE
TECHNICAL LIBRARY
ABBOTTAEROSPACE.COM

Arbitrary geometry, representative of a general aviation aircraft, were employed in the following analysis since the geometry of the aircraft utilized in the Terry drop test was not available. The firewall forces, F_{ux}, F_{uz}, F_{lx}, and F_{lz} were calculated from equations that are based on the free body diagram shown in Figure 41. This free body diagram was drawn with the assumption that the force C_x is assumed to be collinear with F_{lx}.

The forces F_{uz} and F_{lz}, which are assumed to be equal, are determined from the vertical equilibrium equation

$$\sum F_z = m_e \ddot{z}_e = C_z + F_{uz} + F_{lz} - Wt_e \cos\theta \tag{4}$$

where the engine mass, m_e is considered to be 400 lb/g. $\ddot{z}_e$ is the z acceleration of the engine, which can be calculated from the kinematics equation

$$\ddot{z}_e = \ddot{z}_{cg} + (78.0\,in.)\ddot{\theta} \tag{5}$$

where $\ddot{z}_{cg}$ is the z acceleration measured at the lower engine mount (Figure 18) and the distance between the engine cg and the a/c cg is assumed to be 78.0 in. Wt_e denotes the weight of the engine, which is assumed to be $= 400$ lb. Considering $F_z = F_{uz} = F_{lz}$ allows one to solve for these forces, as

$$F_z = \frac{m_e \ddot{z}_e - C_z + Wt_e \cos\theta}{2} \tag{6}$$

THIS DOCUMENT PROVIDED BY THE ABBOTT AEROSPACE
TECHNICAL LIBRARY
ABBOTTAEROSPACE.COM

These solutions are presented in Figures 42 and 43.

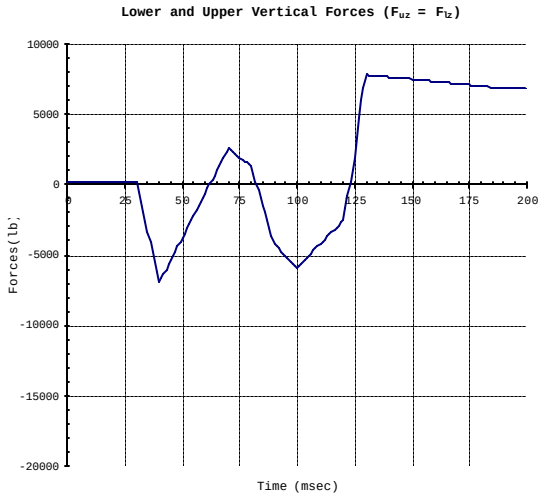

Figure 42. Test 2 Vertical Loads at Lower and Upper Engine Mount Attachment Points

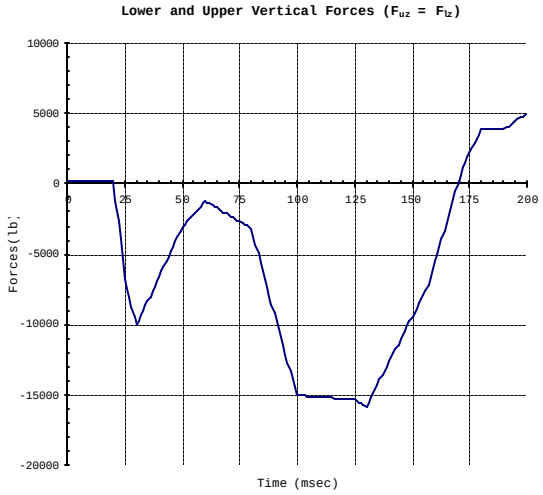

Figure 43. Test 3 Vertical Loads at Lower and Upper Engine Mount Attachment Points

THIS DOCUMENT PROVIDED BY THE ABBOTT AEROSPACE
TECHNICAL LIBRARY
ABBOTTAEROSPACE.COM

Returning to the free body diagram presented in Figure 41, the longitudinal equilibrium equation is written as

$$\sum F_x = m_e \ddot{x} = C_x + F_{ux} + F_{lx} + Wt_e \sin\theta \tag{7}$$

where $\ddot{x}$ represents the average lower engine mount acceleration, which is represented in Figure 12. The total longitudinal force $F_{ux} + F_{lx}$ is calculated as

$$F_{ux} + F_{lx} = m_e \ddot{x} - C_x - Wt_e \sin\theta \tag{8}$$

and is presented in Figures 44 and 45.

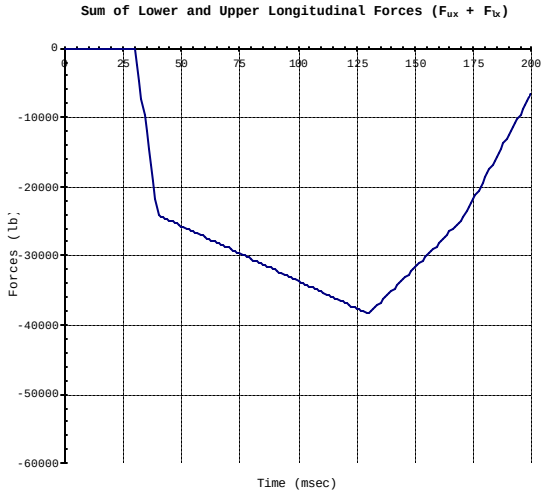

Figure 44. Test 2 Sum of Longitudinal Loads at Lower and Upper Engine Mount Attachment Points

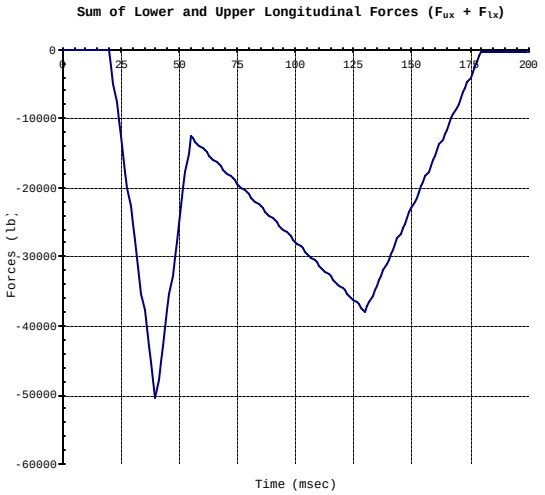

Figure 45. Test 3 Sum of Longitudinal Loads at Lower and Upper Engine Mount Attachment Points

THIS DOCUMENT PROVIDED BY THE ABBOTT AEROSPACE
TECHNICAL LIBRARY
ABBOTTAEROSPACE.COM

The force F_{ux} is determined from the moment equation or

$$\sum M_l = I_{YYe}\ddot{\theta} = dC_z - x_e(Wt_e\cos\theta + m_e\ddot{z}_e) - h(m_e\ddot{x}_e - Wt_e\sin\theta) + bF_{ux} - aF_{uz} \tag{9}$$

where I_{YYe} represents the moment of inertia of the engine about the center of gravity of the engine with respect to the y axis and has been estimated to be 209 lb-in^2/g. Values for the distances a, b, and h are assumed as follows; $a = 9$ in, $b = 23$ in, and $h = 18$ in. The distance between the upper engine mount attachment and the aircraft cg is assumed to be 50.0 in and the distance between the engine cg and the aircraft cg was previously assumed to be 78.0 in. Therefore, $x_e = 28$ in. The distance between the lower engine mount attachment and the impact point, $d = d_x - 59.0$ in., was calculated based on these assumptions. Thus the longitudinal forces acting on the upper engine mount attachment points were calculated using the equation

$$F_{ux} = \frac{I_{YYe}\ddot{\theta} - dC_z + x_e\left(Wt_e\cos\theta + m_e\ddot{z}_e\right) + h(m_e\ddot{x}_e - Wt_e\sin\theta) + aF_{uz}}{b} \tag{10}$$

and are presented in Figures 46 and 47.

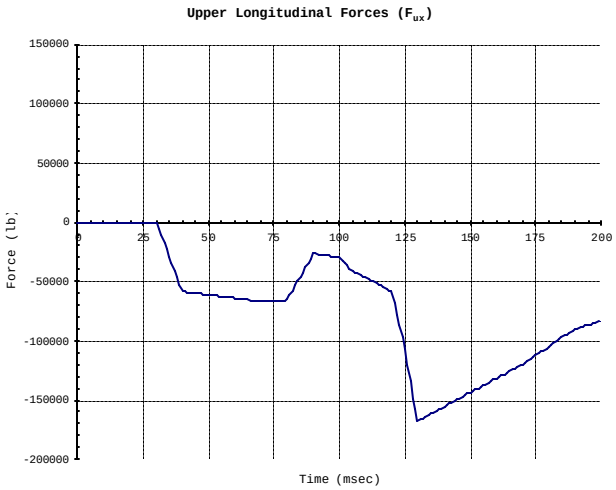

Figure 46. Test 2 Longitudinal Loads at Upper Engine Mount Attachment Points

THIS DOCUMENT PROVIDED BY THE ABBOTT AEROSPACE
TECHNICAL LIBRARY
ABBOTTAEROSPACE.COM

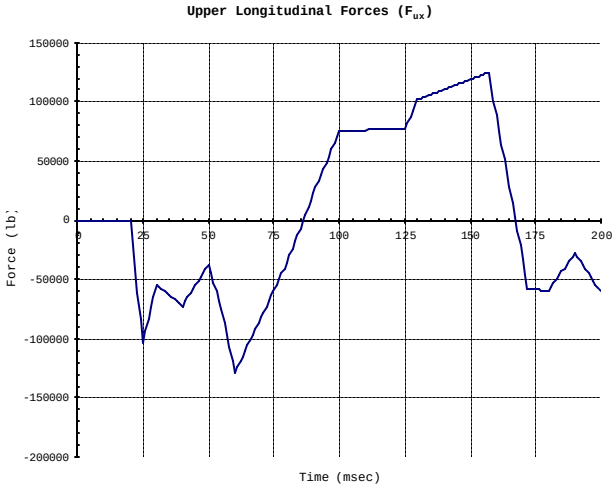

Figure 47. Test 3 Longitudinal Loads at Upper Engine Mount Attachment Points

THIS DOCUMENT PROVIDED BY THE ABBOTT AEROSPACE
TECHNICAL LIBRARY
ABBOTTAEROSPACE.COM

Given this result for F_{ux}, F_{lx} can now be calculated using the longitudinal equilibrium equation (Equation (8)). F_{lx} for Tests 2 and 3 are presented in Figures 48 and 49:

$$F_{lx} = m_e \ddot{x} - C_x - F_{ux} - Wt_e \sin\theta \tag{11}$$

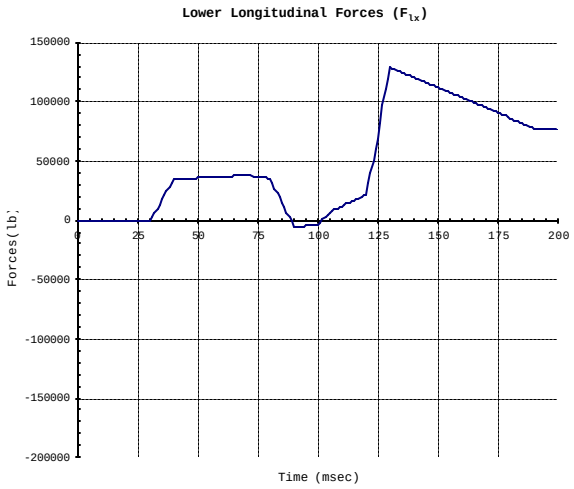

Figure 48. Test 2 Longitudinal Loads at Lower Engine Mount Attachment Points

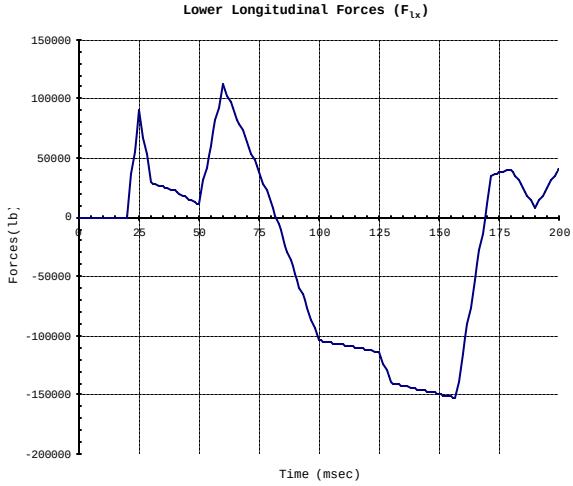

Figure 49. Test 3 Longitudinal Loads at Lower Engine Mount Attachment Points

THIS DOCUMENT PROVIDED BY THE ABBOTT AEROSPACE
TECHNICAL LIBRARY
ABBOTTAEROSPACE.COM

This analysis employs a two-dimensional formulation that combines the forces acting on the left and right sides of the aircraft. Clearly these forces are shared between the appropriate two attachment points. Thus, the vertical loads at each individual engine mount attachment point are calculated using Equation (12) and presented in Figures 50 and 51.

$$F_{uz(right)} = F_{uz(left)} = \frac{1}{2}F_{uz} = F_{lz(right)} = F_{lz(left)} = \frac{1}{2}F_{lz} \tag{12}$$

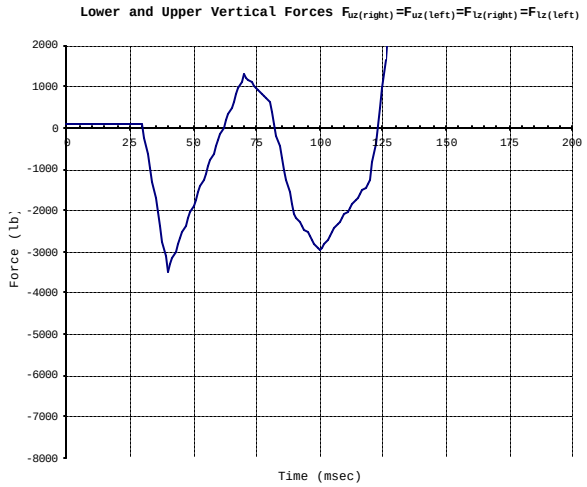

Figure 50. Test 2 Vertical Loads at Each Lower and Upper Engine Mount Attachment Point

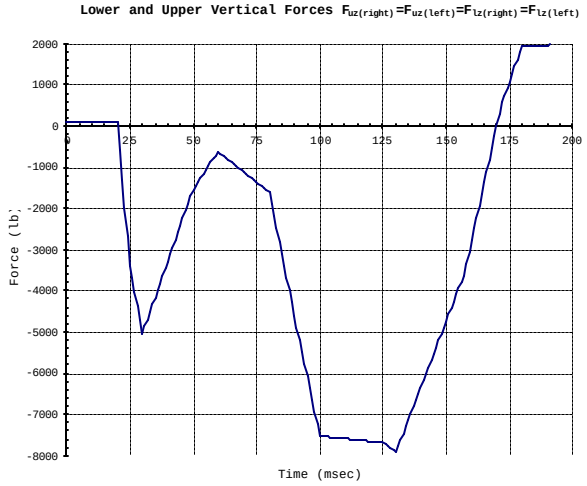

Figure 51. Test 3 Vertical Loads at Each Lower and Upper Engine Mount Attachment Point

THIS DOCUMENT PROVIDED BY THE ABBOTT AEROSPACE
TECHNICAL LIBRARY
ABBOTTAEROSPACE.COM

The longitudinal loads at each of the two upper engine mount attachment points are calculated using Equation (13) and presented in Figures 52 and 53.

$$F_{ux(right)} = F_{ux(left)} = \frac{1}{2} F_{ux} \tag{13}$$

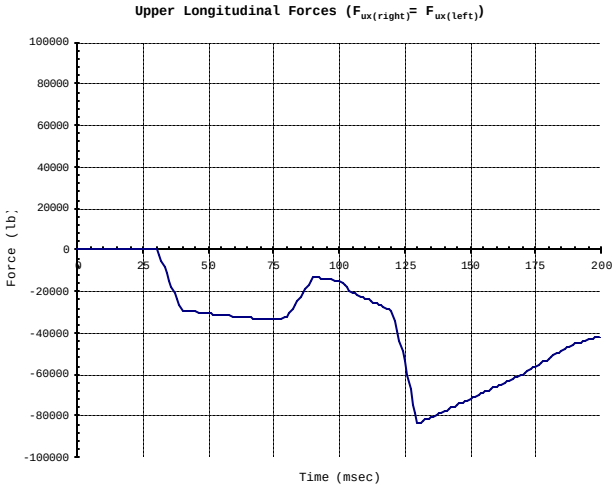

Figure 52. Test 2 Longitudinal Loads at Each Upper Engine Mount Attachment Point

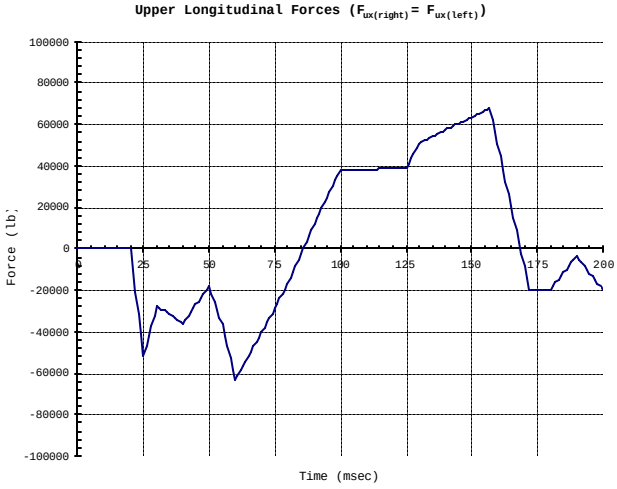

Figure 53. Test 3 Longitudinal Loads at Each Upper Engine Mount Attachment Point

THIS DOCUMENT PROVIDED BY THE ABBOTT AEROSPACE
TECHNICAL LIBRARY
ABBOTTAEROSPACE.COM

The longitudinal loads at each of the two lower engine mount attachment points are calculated using Equation (14) and presented in Figures 54 and 55.

$$F_{lx(right)} = F_{lx(left)} = \frac{1}{2} F_{lx} \tag{14}$$

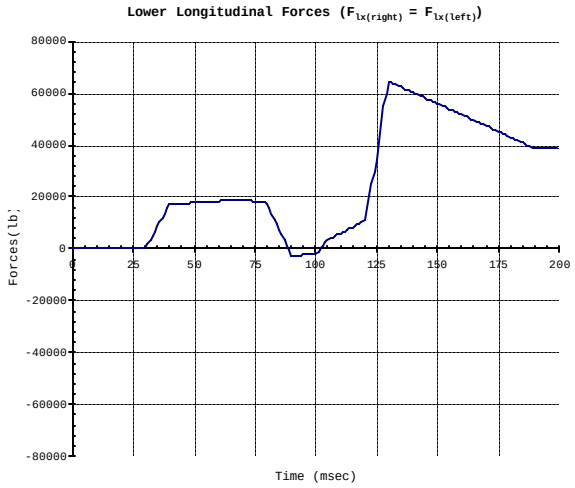

Figure 54. Test 2 Longitudinal Loads at Each Lower Engine Mount Attachment Point

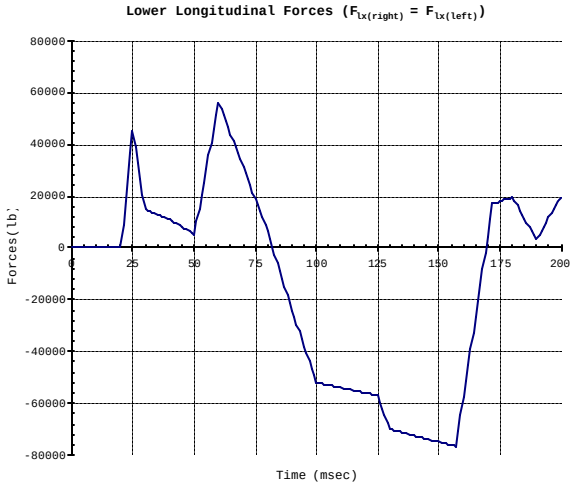

Figure 55. Test 3 Longitudinal Loads at Each Lower Engine Mount Attachment Point

THIS DOCUMENT PROVIDED BY THE ABBOTT AEROSPACE
TECHNICAL LIBRARY
ABBOTTAEROSPACE.COM

Firewall Loads at Initial Impact

Utilizing the longitudinal and vertical load data for Test 2, C_x and C_z, (Figures 13 and 30), Figure 56 presents the calculated resultant load data.

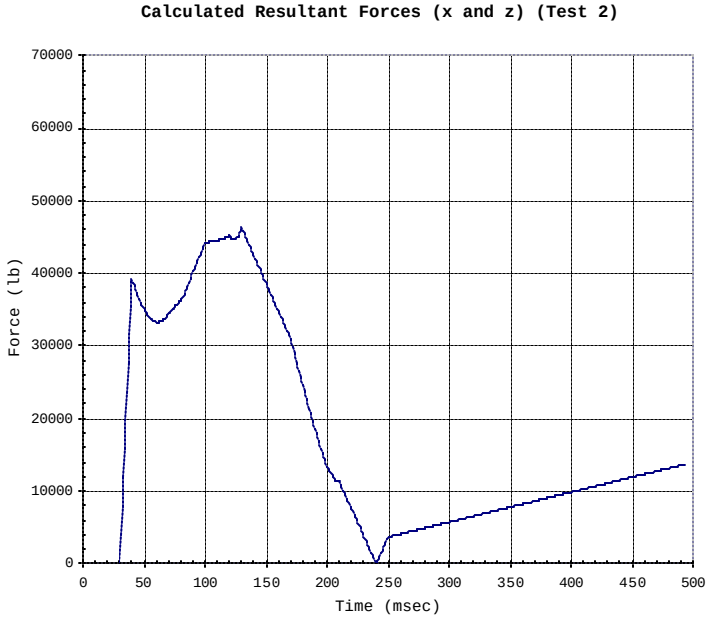

Figure 56. Test 2 Resultant Loads (Longitudinal and Vertical)

It can be observed that the first maximum resultant load occurs at $t = 40$ msec. Referring to the appropriate charts, the following data are observed at that time.

$$C_x = 29{,}000\ lb. \tag{15}$$

$$C_z = 27{,}000\ lb. \tag{16}$$

$$d_x = 120.0\ in. \quad \text{(Defined in Figure 36)} \tag{17}$$

$$F_{uz(right)} = F_{uz(left)} = F_{lz(right)} = F_{lz(left)} = -3{,}475\ lb. \tag{18}$$

$$F_{ux(right)} = F_{ux(left)} = -29{,}275\ lb. \tag{19}$$

$$F_{lx(right)} = F_{lx(left)} = 17{,}200\ lb. \tag{20}$$

THIS DOCUMENT PROVIDED BY THE ABBOTT AEROSPACE
TECHNICAL LIBRARY
ABBOTTAEROSPACE.COM

Utilizing the longitudinal and vertical load data for Test 3, C_x and C_z, (Figures 14 and 31), Figure 57 presents the calculated resultant load data.

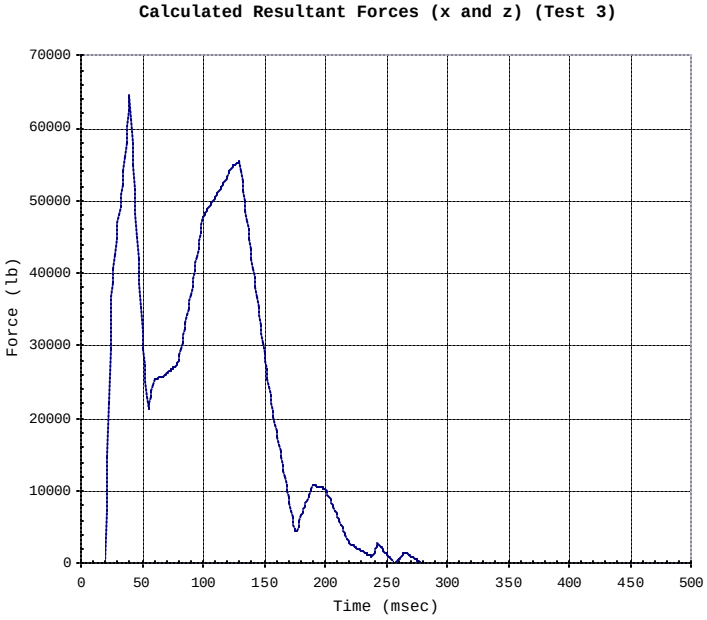

Figure 57. Test 3 Resultant Loads (Longitudinal and Vertical)

It can be observed that the first maximum resultant load occurs at $t = 40$ msec. Referring to the appropriate charts, the following data are observed at that time.

$$C_x = 60{,}000\ lb. \tag{21}$$

$$C_z = 23{,}750\ lb. \tag{22}$$

$$d_x = 143.0\ in. \quad \text{(Defined in Figure 36.)} \tag{23}$$

$$F_{uz(right)} = F_{uz(left)} = F_{lz(right)} = F_{lz(left)} = -3{,}300\ lb. \tag{24}$$

$$F_{ux(right)} = F_{ux(left)} = -36{,}250\ lb. \tag{25}$$

$$F_{lx(right)} = F_{lx(left)} = 11{,}100\ lb. \tag{26}$$

THIS DOCUMENT PROVIDED BY THE ABBOTT AEROSPACE
TECHNICAL LIBRARY
ABBOTTAEROSPACE.COM

These results are used in the definition of longitudinal and vertical load factors to define forces acting on the aircraft cabin. These load factors are based on the airplane gross weight.

For Test 2:

Longitudinal load factor

$$n_x = \frac{-(F_{ux(right)} + F_{ux(left)} + F_{lx(right)} + F_{lx(left)})}{Wt} = \frac{24{,}150\ lb.}{2{,}500\ lb.} = 9.66 \quad (27)$$

Vertical load factor

$$n_z = 1 + \frac{-(F_{uz(right)} + F_{uz(left)} + F_{lz(right)} + F_{lz(left)})}{Wt} = 1 + \frac{13{,}900\ lb.}{2{,}500\ lb.} = 6.56 \quad (28)$$

For Test 3:

Longitudinal load factor

$$n_x = \frac{-(F_{ux(right)} + F_{ux(left)} + F_{lx(right)} + F_{lx(left)})}{Wt} = \frac{50{,}400\ lb.}{2{,}500\ lb.} = 20.16 \quad (29)$$

Vertical load factor

$$n_z = 1 + \frac{-(F_{uz(right)} + F_{uz(left)} + F_{lz(right)} + F_{lz(left)})}{Wt} = 1 + \frac{13{,}200\ lb.}{2{,}500\ lb.} = 6.28 \quad (30)$$

It is interesting to note that the load factors for Test 2 are close to those prescribed for occupants in 14 CFR Part 23.561(b)(2), which specifies a vertical load factor of 3.0 g and a forward load factor of 9.0 g. The definitions differ in that the load factors n_x and n_z are applied simultaneously whereas the load factors specified in 23.561 are applied one at a time.

THIS DOCUMENT PROVIDED BY THE ABBOTT AEROSPACE
TECHNICAL LIBRARY
ABBOTTAEROSPACE.COM

Acknowledgments

The contributions of Hari Balakrishnan and Radhika Vaddepati of the National Institute of Aviation Research at Wichita State University and Steve Soltis of the FAA were very helpful in completing this project.

Conclusions

A simplified analysis technique was formulated to estimate firewall forces for AGATE aircraft designs, based on accelerometer data acquired during full-scale crash tests of similar aircraft. Results are reported for a 30° nose down impact into soft soil at an impact speed approaching $\mathbf{V_{so}}$. These forces represent a new load condition for consideration in the design of the AGATE-class crashworthy aircraft.

The loads predicted by this analysis are conservative since they are based on a rigid body analysis and thus neglect the effects of dissipative forces associated with damage mechanisms, which realistically occur as composite structures respond to these kinds of impact loads. It is important to recognize that the AGATE crashworthiness load condition is only applicable to AGATE-class aircraft, which feature an effective non-plowing, non-scooping firewall, as well as a load-limiting crashworthy engine mount in their design.

Finally, analyses of full-scale drop test data supports the conclusion that the local deformation characteristics of the structure, in this case, the engine mount, do not significantly affect the overall response of the vehicle. This observation should be considered when applying filtering techniques to full-scale dynamic test data.

THIS DOCUMENT PROVIDED BY THE ABBOTT AEROSPACE
TECHNICAL LIBRARY
ABBOTTAEROSPACE.COM

References

1. Terry, J. E., Hooper, S. J., and Nicholson, M., Design and Test of an Improved Crashworthiness Small Composite Airframe - Phase II Report, NASA SBIR Contract NAS1-20427, Terry Engineering, Andover, Kansas, October 1997.
2. Terry, J.E., "Design and Test of an Improved Crashworthiness Small Composite Airplane," SAE Paper 2000-01-1673, Presented at the SAE General Aviation Technology Conference and Exposition, May 9-11, 2000, Wichita, KS.
3. Eiband, A.M., et. al., "Accelerations and Passenger Harness Loads Measured in Full-Scale Light-Airplane Crashes, " NACA TN-2991, 1953.
4. Alfaro-Bou, E., et. al., "Light Airplane Crash Tests at Impact Velocities of 13 and 27 m/sec," NASA TP 1042, 1977.
5. Castle, C.B, et. al., "Light Airplane Crash Tests at Three Roll Angles, " NASA TP 1477, 1979.
6. Vaughan, V.L., et. al., "Crash Tests of Four Identical High-Wing Single-Engine Airplanes," NASA TP 1699, 1980.
7. Vaughan, V.L., et. al., "Light Airplane Crash Tests at Three Pitch Angles," NASA TP 1481, 1979.
8. Williams, S.M., et. al., "Crash Tests of Four Low-Wing Twin-Engine Airplanes With Truss-Reinforced Fuselage Structures," NASA TP 2070, September 1982.
9. Carden, H.D., "Impulse Analysis of Airplane Crash Data with Consideration Given to Human Tolerance," SAE Paper 930748, 1983.
10. Soltis, S. J. and Olcott, J. W., The Development of Dynamic Performance Standards for General Aviation Aircraft Seats, SAE Paper 850853.
11. Aircraft Crash Survival Design Guide, Volume III – Aircraft Structural Crash Resistance, Simula Inc., December 1989.
12. Carden, H.D., "Correlation and Assessment of Structural Airplane Crash Data With Flight Parameters at Impact," NASA TP 2083, 1082.
13. Alfaro-Bou, E. and Castle, C.B., "Crash Tests of Three Identical Low-Wing Single-Engine Airplanes," NASA TP 2190, Washington, D.C., September, 1983.

THIS DOCUMENT PROVIDED BY THE ABBOTT AEROSPACE
TECHNICAL LIBRARY
ABBOTTAEROSPACE.COM

Appendix A - A Survey of Nonlinear Structural Responses Applicable to Crashworthy Designs

Nonlinear structural responses are evident in most energy absorbing systems and are therefore desirable in the design of crashworthy systems. These systems are often idealized as simple elastic-plastic systems but in fact often exhibit more complicated mechanisms that should be considered when analyzing crash test results. These mechanisms assume a variety of forms but are generally associated with the local deformations and can be quite complicated.

Several examples of structures exhibiting significant local effects are presented in this appendix, including the response of an S-Beam Column reported by Khalil [A.1], honeycomb crushing mechanisms [A.2, A.3], a crashworthy subfloor reported by Kindervater [A.4], the response of a cruciform square tube reported by Otubushin [A.5], and crippling failure of thin-walled round tubes reported by Henderson [A.6].

Khalil studied the response of S-Beam Columns, commonly used in the design of automobile chasis, by testing them at diffenent impact velocities. Most of the deformation in these structures is produced in the corners of the frame and much of the inelastic deformation is associated with the local deformations in these locations.

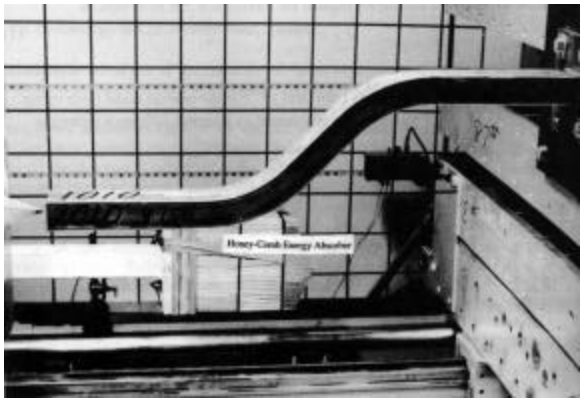

(a) - Pretest Photo

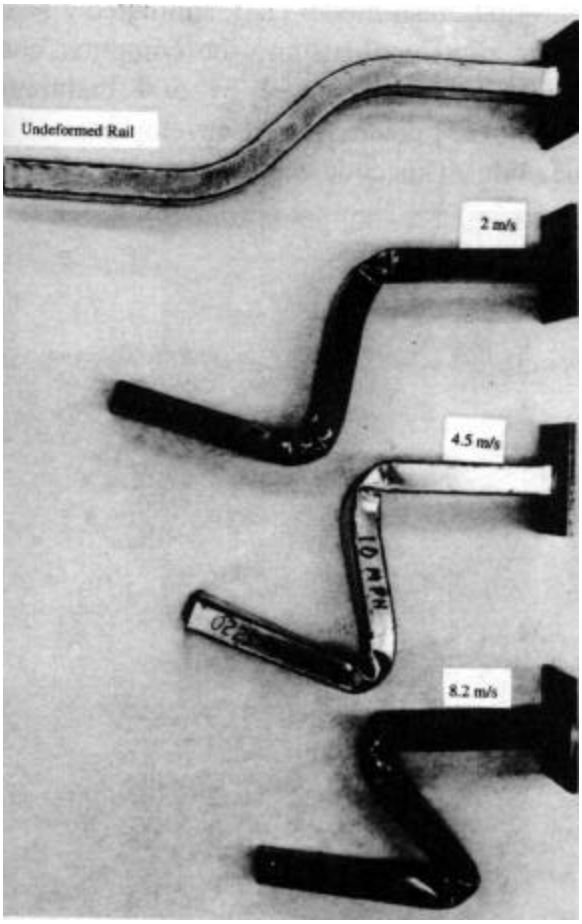

(b) - Permanent Deformations Produced by Tests at Different Impact Velocities

Figure A.1 - Dynamic Sled Tests of S-Beam Columns

THIS DOCUMENT PROVIDED BY THE ABBOTT AEROSPACE
TECHNICAL LIBRARY
ABBOTTAEROSPACE.COM

The measured response for impact velocities ranging between 2 m/s to 8.2 m/s are presented in Fig. A.2. Each of these curves exhibits a damped oscillatory response, which is seen to vary as a function of impact velocity. The reader should recall that the strength of steel is very rate sensitive and may contribute to some of these differences.

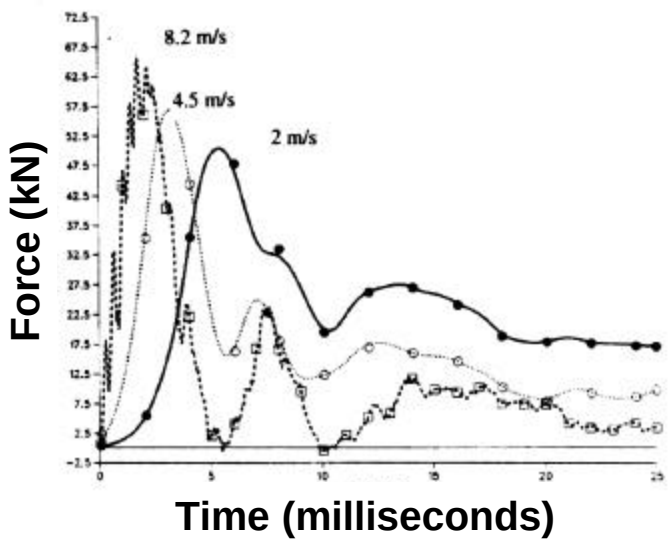

Figure A.2 - Effect of Impact Velocity on Impact Force

The crushing response of honeycomb structures will be considered next. In the following discussion, we are referring to sandwich panel structures consisting of a honeycomb core that is "sandwiched" between two face sheets as shown in Fig. A.3.

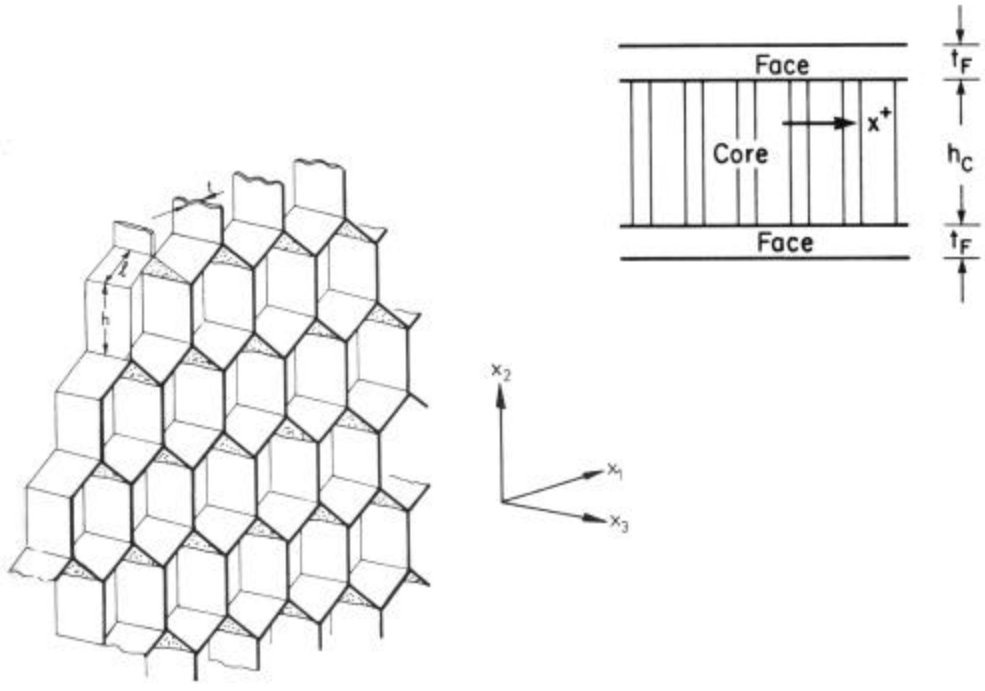

Figure A.3 - Honeycomb Geometry

THIS DOCUMENT PROVIDED BY THE ABBOTT AEROSPACE
TECHNICAL LIBRARY
ABBOTTAEROSPACE.COM

Honeycomb panels exhibit several failure modes, two of which are illustrated in Fig. A.4 below

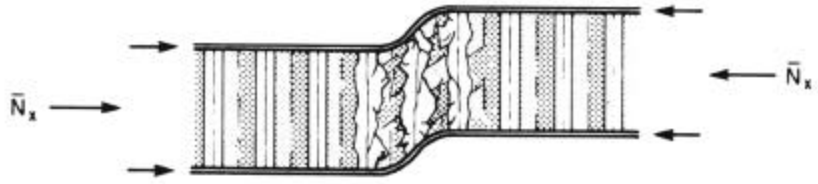

(a) – Core Shear Instability

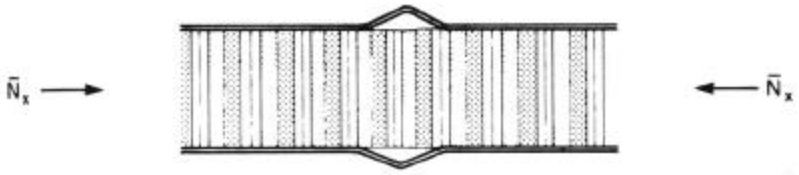

(b) – Face Wrinkling Instability

Figure A.4 - Honeycomb Failure Mechanisms

a generic form of the resulting load-deflection curve is presented in Fig. A.5.

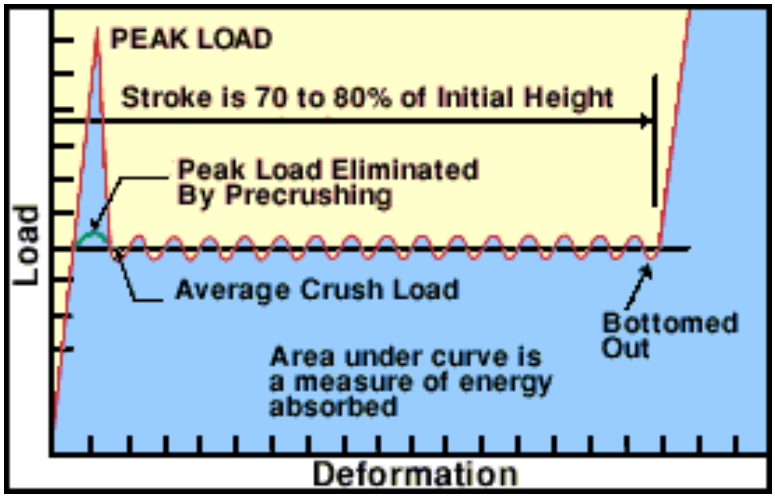

Figure A.5 - Honeycomb Crushing Performance

This response differs from that presented in Fig. A.2 in that it exhibits significant initiation resistance, which is followed by a nearly constant load-deflection response until the system bottoms out. Note, however, that the system also exhibits an oscillatory response in the so-called constant load portion of this curve. Actual data is not always as well behaved as that shown here. This is evident in the test data for stitched panels, shown in Fig. A.6.

THIS DOCUMENT PROVIDED BY THE ABBOTT AEROSPACE
TECHNICAL LIBRARY
ABBOTTAEROSPACE.COM

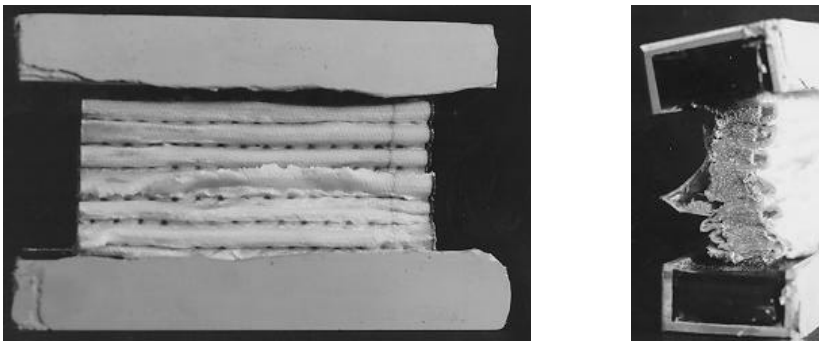

Figure A.6 - Typical Deformation Pattern of Stitched Sandwich Panels

The corresponding load-deflection curve for this specimen is presented in Fig. A.7.

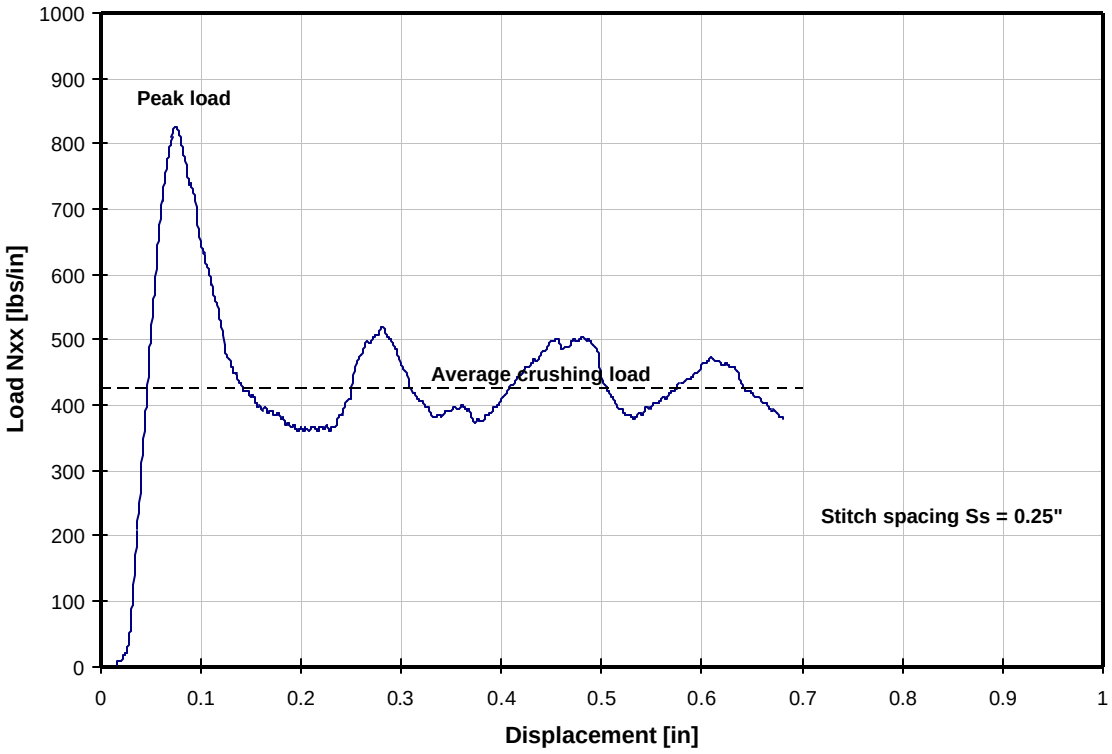

Figure A.7 - Typical Load-Deflection Curve of Stitched Sandwich Panel

THIS DOCUMENT PROVIDED BY THE ABBOTT AEROSPACE
TECHNICAL LIBRARY
ABBOTTAEROSPACE.COM

The energy absorbing subfloor, commonly designed to provide occupant protection in helicopter structures, will be considered as the next example. The structure is presented in Fig. A.8.

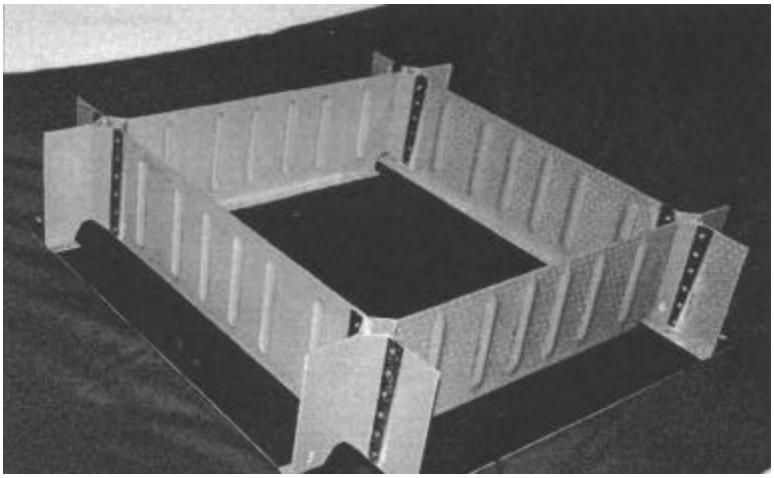

Figure A.8 - Crushable Subfloor

Kindervater [A.4] reported the crushing response of designs with and without cruciforms in the corners, which are reproduced in Fig. A.9. Note that these responses exhibit the same kind of load-deflection response as reported for the previous examples.

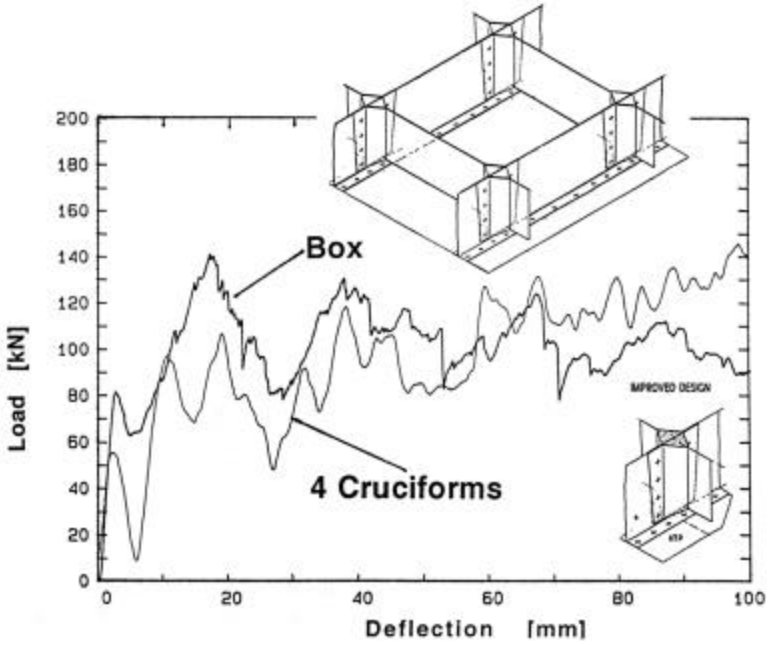

Figure A.9 - Load-Deflection Curve

THIS DOCUMENT PROVIDED BY THE ABBOTT AEROSPACE
TECHNICAL LIBRARY
ABBOTTAEROSPACE.COM

The next example is a simple square tube that is end loaded in compression as illustrated in Fig. A.10. Note that the tube contains imperfections that were formed at specified locations and with specified geometry when the specimen was manufactured.

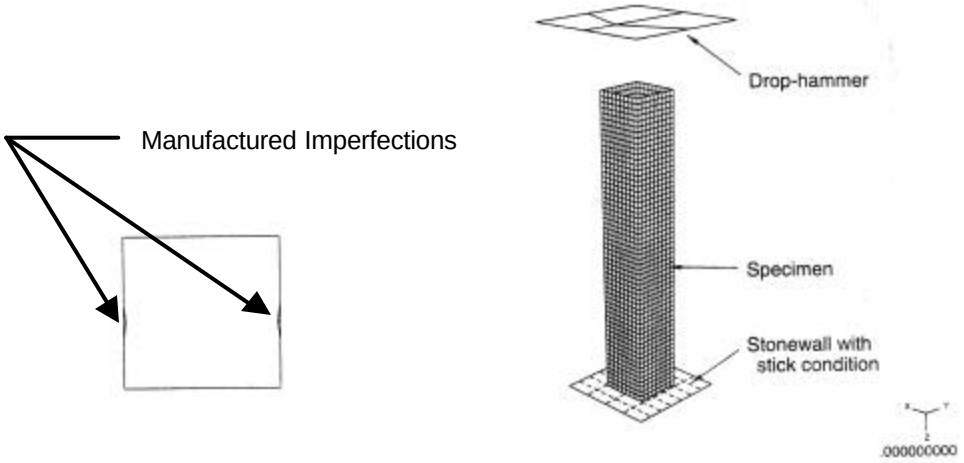

Figure A.10 - Square Tube

Otubushin [A.5] reported the dynamic response of the tube as presented in Fig. A.11 and the measurements presented in Fig. A.12.

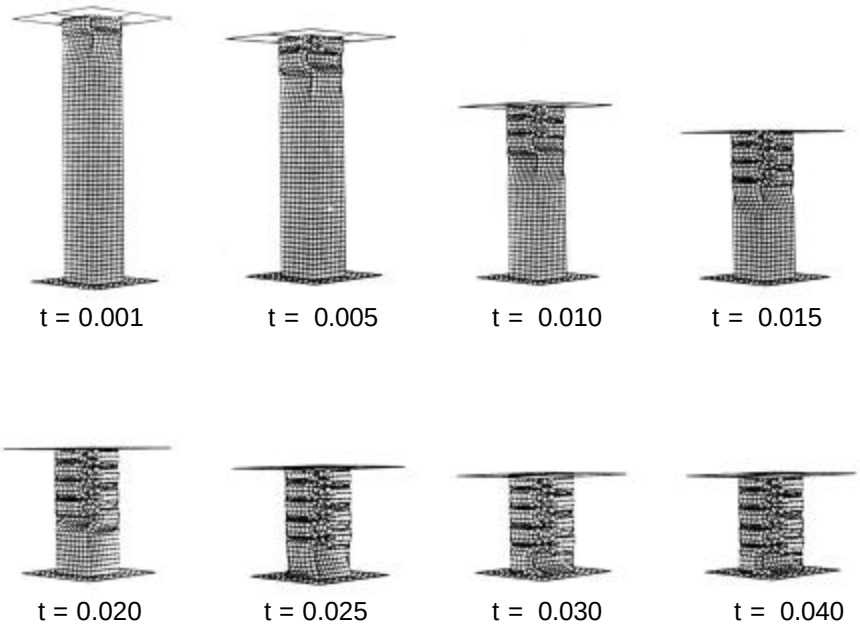

Figure A.11 - Square Tube Response

THIS DOCUMENT PROVIDED BY THE ABBOTT AEROSPACE
TECHNICAL LIBRARY
ABBOTTAEROSPACE.COM

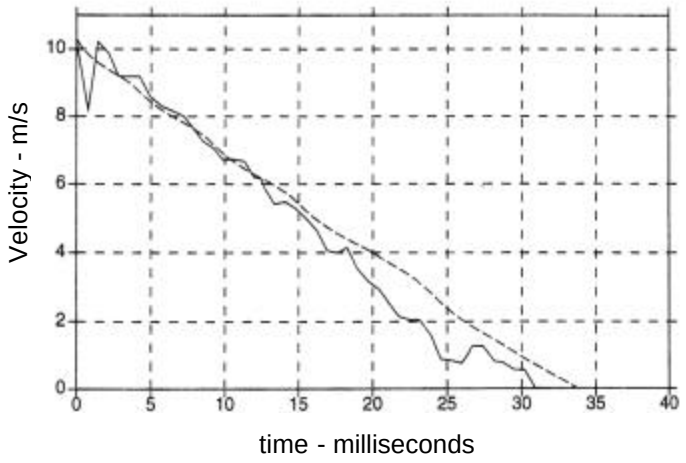

(a) Velocity vs. time

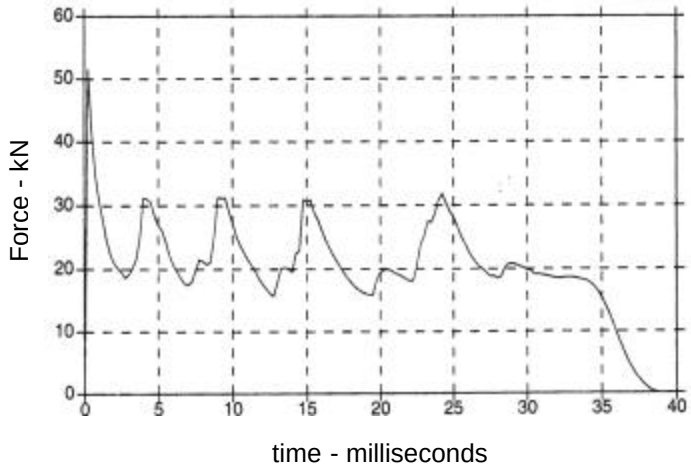

(b) Force vs. time

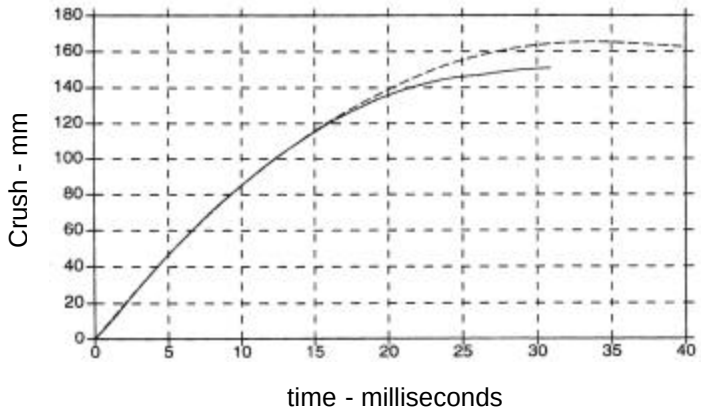

(c) Force vs. time

Figure A.12 - Impact Response of Square Tube

This Document Provided by the Abbott Aerospace
Technical Library
abbottaerospace.com

This structure also exhibits an oscillatory response, shown in Fig. A.12(b). The mechanism producing this oscillation is easily identified. The initial failure initiates at the site of the fabricated imperfections and develops as a local crippling-type failure. The tube crushes in this region and subsequently folds and the magnitude of the load decreases. Eventually the tube folds over onto itself, producing contact forces between the upper and lower portions of the local deformation. This causes the magnitude of the load to increase. This process is repeated a number of times as shown in Fig. A.11.

The last example is a simple round tube that is end loaded in compression similarly to the tube presented in Fig. A.10. Henderson [A.6] reported static response of the tubes presented in Fig. A.13 and the measurements presented in Fig. A.14.

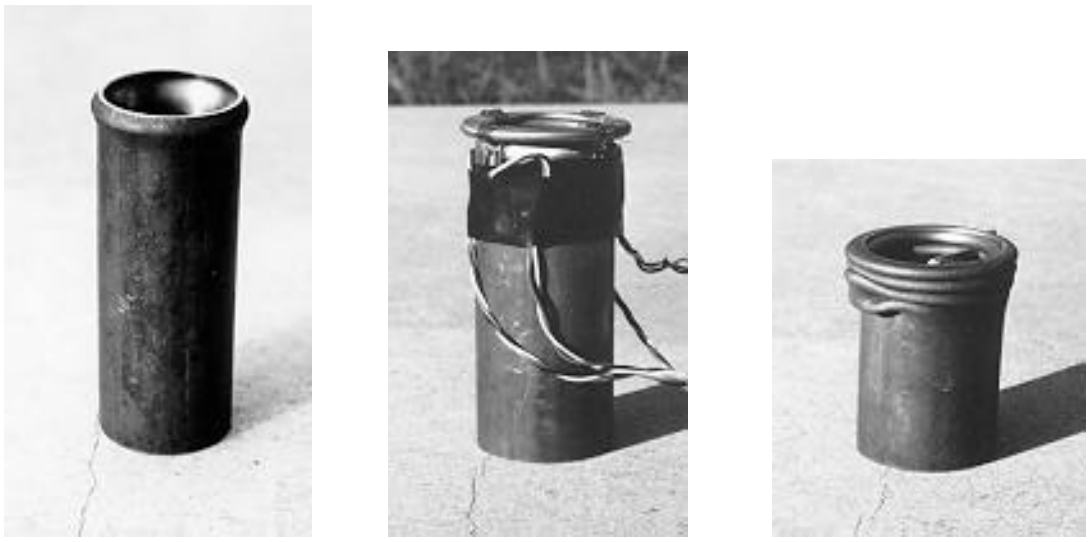

Tube Specimen 1 Tube Specimen 2 Tube Specimen 3

Figure A.13 - Pictures of Tubes after Testing

THIS DOCUMENT PROVIDED BY THE ABBOTT AEROSPACE
TECHNICAL LIBRARY
ABBOTTAEROSPACE.COM

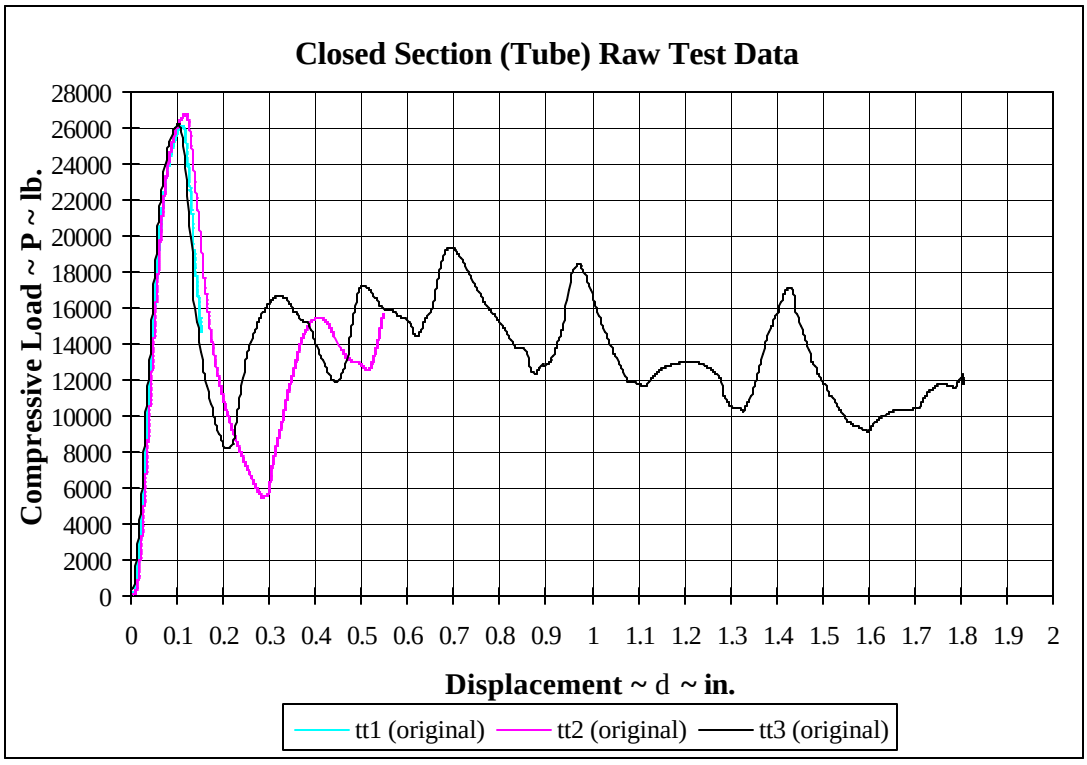

Figure A.14 - Tube Load vs. Displacement Raw Test Data

Again, the oscillatory response is shown. The mechanism producing this oscillation is due to a local crippling-type failure similar to what was described in the previous example.

Clearly, the specific characters of these kinds of nonlinear load-deflection responses are very dependent on the geometry details and material properties of the specimen. However in each case it is possible to identify a primary structural response and a secondary structural response. Thus a measurement may be defined to be the sum of a primary response, a secondary response, and noise (originating in other spurious sources associated with the test apparatus). It is important to note that the specific character of the secondary responses is associated with local geometry, which can vary significantly from design to design.

THIS DOCUMENT PROVIDED BY THE ABBOTT AEROSPACE
TECHNICAL LIBRARY
ABBOTTAEROSPACE.COM

Appendix A - References

A.1. Khalil, T.B., et.al., "Vehicle Crashworthiness and Occupant Protections in Frontal Impact by FE Analysis -- an Integrated Approach," Crashworthiness of Transportation Systems: Structural Impact and Occupant Protection, NATO ASI Series, Ambrosio, J.A.C., Pereira, M.F.O, and da Silva, F.P., Eds., Kluwer Academic Publishers, Dordrecht, The Netherlands, 1997.

A.2. Tomblin, J.S. and Raju, K.S., "Energy Absorption Characteristics of Composite Sandwich Panels Under Compression, AGATE-WP3.3-033012-020-Standard, NASA Langley Research Center, Hampton, VA., October, 1997.

A.3. Vinson, J.R. and Sierakowski, R.L., The Behavior of Structures Composed of Composite Materials, Martinus Nijhoff, Dordrecht, The Netherlands, 1987.

A.4. Kindervater, C.M., "Aircraft and Helicopter Crashworthy Design and Simulation," Crashworthiness of Transportation Systems: Structural Impact and Occupant Protection, NATO ASI Series, Ambrosio, J.A.C., Pereira, M.F.O, and da Silva, F.P., Eds., Kluwer Academic Publishers, Dordrecht, The Netherlands, 1997.

A.5. Otubushin, A., "Detailed Validation of a Non-Linear Finite Element Code Using Dynamic Axial Crushing of a Square Tube," Crashworthiness of Transportation Systems: Structural Impact and Occupant Protection, NATO Advanced Studies Institute, Vol. II Contributed Papers, Ambrosio, J.A.C., Pereira, and M.F.O, Eds., Kluwer Academic Publishers, Dordrecht, The Netherlands, 1997.

A.6. Henderson, M., "Crippling Failure of Thin-Walled Columns: A Comparison of Experimental Data with Nonlinear Finite Element Analysis," Masters Thesis, Wichita State University, Fall, 1997